

Central Lancashire Online Knowledge (CLoK)

Title	Bending waves excited by irregular gas inflow along warps
Туре	Article
URL	https://clok.uclan.ac.uk/id/eprint/41169/
DOI	https://doi.org/10.1093/mnras/stac606
Date	2022
Citation	Khachaturyants, Tigran, Beraldo E silva, Leandro, Debattista, Victor P and Daniel, Kathryne J (2022) Bending waves excited by irregular gas inflow along warps. Monthly Notices of the Royal Astronomical Society, 512 (3). pp. 3500-3519. ISSN 0035-8711
Creators	Khachaturyants, Tigran, Beraldo E silva, Leandro, Debattista, Victor P and Daniel, Kathryne J

It is advisable to refer to the publisher's version if you intend to cite from the work. https://doi.org/10.1093/mnras/stac606

For information about Research at UCLan please go to http://www.uclan.ac.uk/research/

All outputs in CLoK are protected by Intellectual Property Rights law, including Copyright law. Copyright, IPR and Moral Rights for the works on this site are retained by the individual authors and/or other copyright owners. Terms and conditions for use of this material are defined in the http://clok.uclan.ac.uk/policies/

MNRAS **512**, 3500–3519 (2022) Advance Access publication 2022 March 7



Downloaded from https://academic.oup.com/mnras/article/512/3/3500/6543710 by University of Central Lancashire user on 13 April 2022

Bending waves excited by irregular gas inflow along warps

Tigran Khachaturyants [®], ¹★ Leandro Beraldo e Silva [®], ^{1,2} Victor P. Debattista [®] 1 and Kathryne J. Daniel [®] 3

Accepted 2022 March 2. Received 2022 February 28; in original form 2021 October 19

ABSTRACT

Gaia has revealed clear evidence of bending waves in the vertical kinematics of stars in the solar neighbourhood. We study bending waves in two simulations, one warped, with the warp due to misaligned gas inflow, and the other unwarped. We find slow, retrograde bending waves in both models, with the ones in the warped model having larger amplitudes. We also find fast, prograde bending waves. Prograde bending waves in the unwarped model are very weak, in agreement with the expectation that these waves should decay on short, approximately crossing, time-scales, due to strong winding. However, prograde bending waves are much stronger for the duration of the warped model, pointing to irregular gas inflow along the warp as a continuous source of excitation. We demonstrate that large-amplitude bending waves that propagate through the solar neighbourhood give rise to a correlation between the mean vertical velocity and the angular momentum, with a slope consistent with that found by Gaia. The bending waves affect populations of all ages, but the sharpest features are found in the young populations, hinting that short-wavelength waves are not supported by the older, kinematically hotter, populations. Our results demonstrate the importance of misaligned gas accretion as a recurrent source of vertical perturbations of disc galaxies, including in the Milky Way.

Key words: stars: kinematics and dynamics – Galaxy: disc – Galaxy: kinematics and dynamics – solar neighbourhood – Galaxy: structure – galaxies: evolution.

1 INTRODUCTION

Early hints that the solar neighbourhood (SN) is vertically perturbed (Gómez et al. 2012; Widrow et al. 2012; Carlin et al. 2013; Williams et al. 2013; Yanny & Gardner 2013; Faure, Siebert & Famaey 2014) have been dramatically confirmed with the Gaia data. Already by using just the Tycho-Gaia data release (DR) 1 astrometric solution (TGAS) data set (Gaia Collaboration 2016a, b), Schönrich & Dehnen (2018) (hereafter, SD18) found a linear increase in the mean vertical velocity, $\langle v_z \rangle$, with the azimuthal velocity, v_{ϕ} , angular momentum, L_{z} , and guiding radius, R_{g} , of stars in the SN. Since the line of nodes (LONs) of the Galactic warp is only $\sim 17.5^{\circ}$ ahead of the Sun (Chen et al. 2019), this linear increase is potentially the warp's direct imprint on the local stellar kinematics. SD18 only used stars along narrow cones in the centre and anticentre directions to obtain v_z and v_{ϕ} without requiring radial velocity measurements, which the TGAS data set lacks. SD18 also noted the presence of a wave-like pattern imprinted on the overall $\langle v_z \rangle$ distribution, towards both the centre and anticentre directions. A smooth, monotonic warp would not present such a signal; instead, SD18 obtained a good fit with a simple sinusoidal wave, as might be produced by a winding warp or by a bending wave. Subsequently, this pattern in $\langle v_z \rangle$ was replicated by Huang et al. (2018) (hereafter, H18) using an $\sim 10^5$ -star sample from the LAMOST-TGAS data. Unlike the TGAS sample, LAMOST-

TGAS has full 6D phase-space measurements, which allowed H18 to replicate the wave-like pattern in $\langle v_z \rangle$ versus L_z and versus v_ϕ in the entire SN. With the release of *Gaia* DR2, the linear increase and wave-like pattern in $\langle v_z \rangle$ were again confirmed by Friske & Schönrich (2019).

Subsequently, *Gaia* DR2 revealed a phase-space spiral in the (z, v_z) plane. Antoja et al. (2018) selected $\sim 9 \times 10^5$ stars in the solar annulus of the *Gaia* DR2 radial velocity sample (RV), which contains the full 6D phase-space coordinates (Gaia Collaboration 2018), and projected them on to the (z, v_z) plane. The result was a spiral with one complete wrap, with a trailing tail reaching up to $\sim 700\,\mathrm{pc}$ and $\sim 40\,\mathrm{km\,s^{-1}}$ in |z| and $|v_z|$, respectively. This phase-space spiral is particularly apparent when colour coded by the azimuthal velocity, v_ϕ , implying a coupling between the in-plane and vertical motions. The presence of this phase-space spiral indicates that the SN is undergoing vertical phase mixing as a result of vertical perturbations (Antoja et al. 2018). The *Gaia* phase-space spiral was dissected by Li & Shen (2020), who showed that it is weaker for stars on radially hotter orbits.

The cause of these vertical perturbations in the SN remains uncertain. In general, vertical perturbations in galactic discs propagate as bending waves (Hunter & Toomre 1969; Merritt & Sellwood 1994; Sellwood 1996; Sellwood, Nelson & Tremaine 1998; Kazantzidis et al. 2009; Chequers, Widrow & Darling 2018; Bland-Hawthorn et al. 2019; Darling & Widrow 2019; Khoperskov et al. 2019) with many possible causes. Widrow et al. (2012) presented evidence for a wave-like perturbation in the Galactic disc in the form of the

¹Jeremiah Horrocks Institute, University of Central Lancashire, Preston PR1 2HE, UK

²Department of Astronomy, University of Michigan, 1085 South University Avenue, Ann Arbor, MI 48109, USA

³Department of Physics, Bryn Mawr College, Bryn Mawr, PA 19010, USA

^{*} E-mail: astrotkh@gmail.com

Galactic north—south asymmetry, speculating that it could have come about via satellite interactions. Feldmann & Spolyar (2014) used a high-resolution numerical simulation to study the interactions of dark matter substructure with the disc and observed that subhalo interactions resulted in distinct and coherent variations in the vertical velocities of disc stars. Gómez et al. (2017) presented multiple high-resolution cosmological simulations of individual Milky Way (MW)-sized galaxies that develop significant vertical bending waves via satellite interactions.

The Sagittarius dwarf galaxy (Sgr) is the most frequently invoked external cause of vertical excitation of the MW's disc (Dehnen 1998; Ibata & Razoumov 1998; Laporte et al. 2019), due to its relatively recent (\sim 0.4–1 Gyr ago) passage through the disc and an orbit that is perpendicular to the Galactic plane (Ibata & Razoumov 1998; Laporte et al. 2019). Sgr has also been suggested to be the cause of the bending wave observed by SD18 and H18. The analysis of the phase-space spiral led Antoja et al. (2018) to infer that the Galactic disc was perturbed in the past 300–900 Myr, which matches current estimates of a pericentric passage by Sgr. Li & Shen (2020) presented further support for the Sgr scenario with a vertically perturbed test particle simulation. They estimated that the perturbation should have happened at least 500 Myr ago to observe the Gaia phase-space spiral in its current form. However, other simulations have shown inconsistencies in the Sgr scenario. Binney & Schönrich (2018) produced a phase-space spiral in an SN population extracted from a distribution function fitted to Gaia DR2 RV and estimated that the spiral formed $400 \pm 150 \, \mathrm{Myr}$ ago. While their time-scale estimate is in some agreement with Antoja et al. (2018)'s results, the mass and duration of the interaction required to produce similar phasespace spirals were significantly higher and faster, respectively. In a pure *N*-body simulation, Bland-Hawthorn & Tepper-García (2021) have shown that the current mass estimate of the Sgr dwarf is too low to excite the phase spiral. Instead, Bland-Hawthorn & Tepper-García (2021) suggested that the interaction had to have happened 1-2 Gyr ago with the Sgr dwarf losing mass at a high rate. Additionally, Bennett & Bovy (2021) used one-dimensional (vertical) models of satellite-disc interaction and were unable to reproduce the observed asymmetry in the vertical number counts for any plausible combination of Sgr and MW properties.

On the other hand, Chequers et al. (2018) showed that isolated galaxies can also self-excite bending waves. Their N-body simulations of isolated galaxies naturally develop bending waves not just when the halo is clumpy but also when it is a smooth distribution of a finite number of dark matter particles. The bending waves in both kinds of simulations have a similar morphology and frequencies, but differ in amplitude, with the clumpy halo exciting waves of higher amplitudes. In the smooth halo models, the bending waves were seeded by the random noise of the halo and bulge particle distributions (Chequers & Widrow 2017). In the clumpy halo models, instead, the subhaloes imprint local perturbations on the disc that then shear into bending waves. The buckling of a galactic bar also induces bending waves in the disc. Khoperskov et al. (2019) presented a high-resolution N-body simulation that developed a bar that then buckled; i.e. it suffered a vertical bending instability of the bar (Raha et al. 1991; Sellwood & Merritt 1994). The resulting bending waves propagated outwards in the disc and remained coherent for a long time, with the phase-space spirals still being distinguishable 3 Gyr after the bar buckled. However, it is unclear whether the MW's bar could have buckled this recently without scattering too many relatively young stars into the bulge (Debattista et al. 2019).

An alternative mechanism for generating vertical bending waves comes from the observation that, in galaxy formation simulations, gas reaches the disc with a misaligned angular momentum (Binney & May 1986; Ostriker & Binney 1989; van den Bosch et al. 2002; Roškar et al. 2010; Velliscig et al. 2015; Stevens et al. 2017; Earp et al. 2019), regardless of whether it settles to the disc via hot or cold modes. Such angular momentum misalignments cause long-lived warps, as opposed to the transient warps excited by interactions (Ostriker & Binney 1989; Roškar et al. 2010; Aumer et al. 2013). In the presence of a live dark halo, the assumption of steady warp precession (Dekel & Shlosman 1983; Toomre 1983) fails as warps in N-body simulations rapidly wind up (Binney, Jiang & Dutta 1998). However, even in the presence of a live halo, misaligned accretion could still create warps with amplitudes comparable to those of observed warps (Jiang & Binney 1999). These warps provide another mechanism by which the disc may be vertically excited, as shown by Gómez et al. (2017), who found that some of their cosmological simulations had prominent vertical bends in discs with no recent satellite interaction. They argued that these bends are most prominent in the youngest stellar populations (< 2 Gyr) and cold gas, and almost absent in the oldest stars. The MW's H I disc has long been known to be warped (Kerr 1957; Weaver & Williams 1974; Levine, Blitz & Heiles 2006), with the warp reaching ≥4 kpc above the mid-plane at R = 25 kpc. A warp has also been observed in the stellar component of the Galactic disc (Efremov, Ivanov & Nikolov 1981; Reed 1996; López-Corredoira et al. 2014). Recently, with the help of the WISE catalogue of periodic variable stars (Chen et al. 2018), the stellar warp has also been mapped in greater detail in the young stellar populations (Chen et al. 2019).

This paper uses *N*-body + SPH (smooth particle hydrodynamics) simulations to explore a scenario in which bending waves are induced by gas accreting along a warp. In Paper I (Khachaturyants, Beraldo e Silva & Debattista 2021), we used the same warped simulation to show that if the MW's warp is formed by misaligned gas accretion, then stars formed in the warp could migrate inwards and be found in the SN. The paper is organized as follows: We describe a warped and a control unwarped simulation in Section 2. The evolution of the warp is described in Section 3. In Section 4, we analyse the bending waves that develop in both the warped and unwarped simulations, comparing and contrasting them. Lastly, we summarize our results in Section 5.

2 SIMULATIONS

We construct two simulations, one with and one without a warp, in order to study the effect of warps on generating bending waves. Hereafter, we refer to the simulations as the warped and unwarped models.

2.1 The warped model simulation

The warped model has the same initial conditions as the simulation used in Khachaturyants et al. (2021) and is produced via the method of Debattista et al. (2015), which constructs triaxial dark matter models with gas angular momentum misaligned with the principal axes of the halo. Aumer & White (2013) showed that inserting rotating gas coronae within non-spherical dark matter haloes leads to a rapid and substantial loss of gas angular momentum. To avoid this catastrophic angular momentum loss, our approach includes adiabatic gas already while merging haloes to produce a non-spherical system. We merge two identical spherical Navarro–Frenk–White (Navarro, Frenk & White 1996) dark matter haloes, each having a co-spatial gas corona comprising 10 per cent of the total mass. The mass and virial radius of each dark matter halo at z =

0 are set to $M_{200} = 8.7 \times 10^{11} \,\mathrm{M}_{\odot}$ and $r_{200} = 196 \,\mathrm{kpc}$, respectively. The gas is in pressure equilibrium within the global potential. Gas velocities are initialized to give a spin parameter of $\lambda = 0.16$ (Bullock et al. 2001), with specific angular momentum $i \propto R$, where R is the cylindrical radius. Both the dark matter halo and the gas corona are comprised of 10⁶ particles. Gas particles start out with masses of $1.4 \times 10^5 \,\mathrm{M_\odot}$ and softening $\epsilon = 20 \,\mathrm{pc}$, while dark matter particles have two different mass configurations (10⁶ and $3.6 \times 10^6 \,\mathrm{M_\odot}$ inside and outside 200 kpc, respectively) and $\epsilon = 100$ pc. The two haloes are placed 500 kpc apart and approach each other head-on at 100 km s⁻¹. If the direction of the separation vector (and the relative velocity) is the x-axis and the haloes are rotating about their z-axes, a tilt about the y-axis is applied to one of the haloes so that the final system will be prolate with its long axis along the x-axis and a gas angular momentum tilted with respect to the symmetry axes of the halo.

This simulation is evolved with the SPH code GASOLINE (Wadsley, Stadel & Quinn 2004), with a base time-step $\Delta t = 10\,\mathrm{Myr}$. This time-step is refined for individual particles such that each particle satisfies the condition $\delta t = \Delta t/2^n < \eta \sqrt{\epsilon/a_\mathrm{g}}$, where a_g is the acceleration at the particle's current position, with $\eta = 0.175$. The opening angle of the tree code calculation is set to $\theta = 0.7$.

The result of this set-up is a dark matter halo with $r_{200}=238\,\mathrm{kpc}$ and $M_{200}=1.6\times10^{12}\,\mathrm{M}_\odot$, and gas with $\lambda=0.11$. These are the initial conditions of the warped simulation. At this stage, we turn on gas cooling, star formation, and stellar feedback using the blastwave prescriptions of Stinson et al. (2006). Gas particles form stars with a 10 per cent efficiency if a gas particle has number density $n>1\,\mathrm{cm}^{-3}$ and temperature $T<15\,000\,\mathrm{K}$ and is part of a convergent flow.

Star particles form with an initial mass that is one-third of the initial parent gas particles, corresponding to $4.6 \times 10^4 \,\mathrm{M_\odot}$ at our resolution. The star particles all have $\epsilon = 20 \,\mathrm{pc}$. Once a gas particle loses 80 per cent of its initial mass, the remaining mass is distributed among the nearest neighbouring gas particles, leading to a decreasing number of gas particles. Star particles are represented by an entire stellar population with a Miller-Scalo (Miller & Scalo 1979) initial mass function. The evolution of star particles includes asymptotic giant branch stellar winds and feedback from Type II and Type Ia supernovae, with their energy injected into the interstellar medium (ISM). Each supernova releases 1050 erg into the ISM. The time-steps of gas particles satisfy the additional condition $\delta t_{\rm gas} = h \, \eta_{\rm courant} / [(1 + \alpha)c + \beta \, \mu_{\rm max}],$ where h is the SPH smoothing length, $\eta_{\text{courant}} = 0.4$, $\alpha = 1$ is the shear coefficient, $\beta = 2$ is the viscosity coefficient, c is the sound speed, and μ_{max} is the maximum viscous force measured between the gas particles (Wadsley et al. 2004; Springel 2010). The SPH kernel uses the 32 nearest neighbours. Gas metallicity is taken into account in the gas cooling process using the prescriptions of Shen, Wadsley & Stinson (2010); to prevent the cooling from dropping below our resolution, we set a pressure floor on gas particles of $p_{\text{floor}} = 3G\epsilon^2 \rho^2$, where G is Newton's gravitational constant and ρ is the gas particle's density (Agertz, Teyssier & Moore 2009).

2.2 The unwarped simulation

The unwarped model is the M1_c_b simulation described in Fiteni et al. (2021). Briefly, the model is similar to one of the spherical models we start with in the warped simulation, except that the initial gas angular spin is $\lambda = 0.065$ (Bullock et al. 2001). Feedback via supernova explosions again employs the blastwave prescription (Stinson et al. 2006). The main difference between this and the

warped simulation (aside from the initial conditions) is that we use a gas particle softening of 50 pc, the star formation efficiency is 5 per cent, and the feedback from supernovae is set to 4×10^{50} erg per supernova.

2.3 Pre-processing the simulations

Simulation snapshots are saved every 10 Myr and are processed through our custom PYTHON library suite (Khachaturyants et al. 2021). The processing involves centring the galactic disc and then rotating it into the (x, y) plane based on the angular momentum of the inner stellar disc $(R < 5 \,\mathrm{kpc})$ for both models. After this reorientation, the warped model is rotated such that the maximum vertical displacement of the tilted ring model (Briggs 1990), i.e. the warp's major axis (WMA), is on the x-axis and, consequently, the LONs is on the y-axis. Lastly, the disc is rotated by 180° about the y-axis, which results in a sense of rotation (clockwise when viewed from the positive z-axis, hereafter the North Galactic pole) and warp orientation similar to that of the MW (Chen et al. 2019). We define an azimuthal angle coordinate ϕ_w , where $\phi_w=0$ represents the ascending node of the LON (y < 0 axis), and increases in the direction of rotation. As a result, the gas warp in each snapshot reaches its peak negative value along the positive x-axis, i.e. $\phi_w = -90^\circ$. In the case of the unwarped model, the process is repeated without the WMA reorientation, so we define $\phi = 0$ as being along the x-axis.

The rotation curves of the two models at 12 Gyr are presented in Fig. 1. Potentials for both simulations were interpolated using the AGAMA software library (Vasiliev 2019) using a single multipole approximation for the stellar, gas, and dark particles combined. Rotation curves of the interpolated potentials are presented in Fig. 1 as dashed red lines. As in the MW, the rotation curves of the two models are relatively flat, though the unwarped model has a higher stellar density in the centre and therefore a peak in the rotation curve at \sim 1 kpc.

3 WARP EVOLUTION

The top row of Fig. 2 presents edge-on views of stars (colour) and the cool ($T_{\rm g} \leq 50\,000$ K) gas (red contours) between t=3 and 12 Gyr. Throughout the evolution of the warped model, gas is accreting on to the disc along an integral-shaped warp. By 12 Gyr, the gas warp extends up to 15 kpc above the plane at $R\sim 20$ kpc. Because of our re-orientation of the disc, the major axis of the warp is along the x-axis and reaches a peak negative value along the x>0 side; in reality, viewed from an inertial frame the disc is tilting slowly and continuously during this time (Binney & May 1986; Ostriker & Binney 1989; Debattista et al. 2015; Earp et al. 2017, 2019) but we subtract this tilting.

In order to study the evolution of the warp, we construct Briggs figures (Briggs 1990) for the warped and unwarped models. A Briggs figure represents warping by means of the spherical azimuthal and inclination angles, ϕ_J and θ_J , respectively, between the total angular momenta of concentric annuli and the z-axis. These are then plotted as the radial, ρ (for θ_J), and angular, ψ (for ϕ_J), variables of a two-dimensional polar plot. Because we reorient the discs into the (x, y) plane based on the angular momentum of the inner disc stars before we perform any analysis, the inner disc is at the origin of the Briggs figures, i.e. it has angular momentum along the z-axis. The bottom row of Fig. 2 shows Briggs figures for the warped model at the same time intervals. The figure presents the stars (in black) and the cool gas (in red) separately. The stellar and gaseous discs are divided into annuli of width $\Delta R = 0.5$ kpc, and then we calculate the total

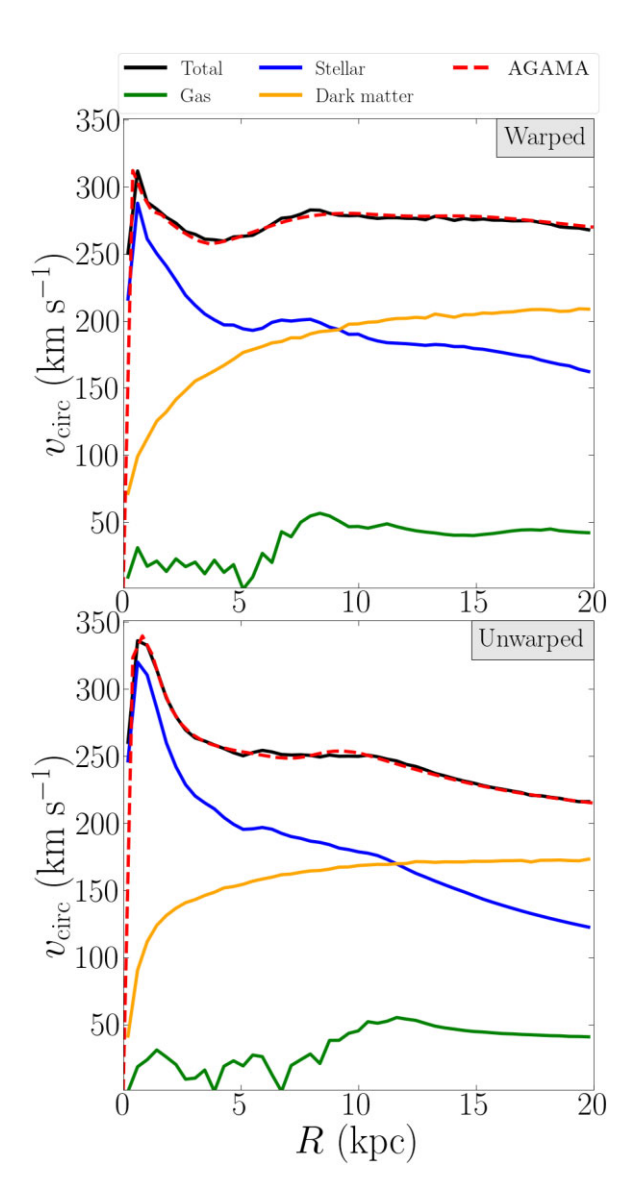


Figure 1. Rotation curves for the warped (top) and unwarped (bottom) models at 12 Gyr. Solid lines represent the rotation curves of each galactic component (computed for each family of particles using the PROFILE function of the PYNBODY library; Pontzen et al. 2013), while the interpolated total potential (computed with AGAMA; Vasiliev 2019) is represented by the dashed red lines.

angular momentum of particles in each annulus. A warp is present in the gas component throughout the evolution of the warped model. The warp grows slowly with time; by 12 Gyr, it extends to almost 40° . The warp traces a leading spiral relative to the sense of rotation of the disc, in agreement with Briggs's third rule of warp behaviour (Briggs 1990) that states that, beyond a certain radius, the LON lies along a loosely wound, leading spiral. On the other hand, the stellar component loses its large-scale warp after 6 Gyr, and only a small stellar warp remains.

In contrast, a similar analysis on the unwarped model does not reveal any notable disc warping. In the top row of Fig. 3, the edge-on views of the unwarped model present no stellar (colour) or gaseous (red contours) warps at any point in time. The bottom row of Fig. 3 shows similar Briggs figures as in Fig. 2 but with significantly smaller $\theta_{\rm L}$ upper limits to underline the lack of warping in the unwarped model. We observe no warping in the stellar component at all times and only minor tilting at $R=10\,{\rm kpc}$ at 6 and 9 Gyr for the gas.

Fig. 4 presents cold gas and stellar profiles for both models at $t=12\,\mathrm{Gyr}$ in the surface density (top panel) and their inclination (bottom panel). The unwarped model exhibits a drop in the gas surface density at the edge (10 kpc) while the inclination of both stellar and gas components remains flat throughout the disc and its outskirts. In the warped model, we observe a slower decline in the surface density of both components, with the stellar disc showing a weak increase in inclination, caused by newly ($\leq 2\,\mathrm{Gyr}$) formed warp stars. The inclination of the gas disc rapidly grows from $r\geq 9\,\mathrm{kpc}$ and reaches $\theta_{\rm L}\sim 40^\circ$ by $r\geq 15\,\mathrm{kpc}$.

4 BENDING WAVES

4.1 The presence of vertical bends

Fig. 5 shows the stellar distributions in the x-y (top) and $R-\phi_w$ (bottom) planes of the average height, $\langle z \rangle$ (left), and the average vertical velocity, $\langle v_z \rangle$ (right), in the warped and unwarped models (see top left annotation). The distributions highlight the presence of large-scale bends (coherent blue and red structures) in the disc. The warped model exhibits bends with amplitudes of $\sim 100\,\mathrm{pc}$ and $\sim 3\,\mathrm{km\,s^{-1}}$ for $\langle z \rangle$ and $\langle v_z \rangle$, respectively, that reach far inside the disc down to $R\simeq 2\,\mathrm{kpc}$. In agreement with Chequers et al. (2018), bends are also observed in the unwarped model, but are noticeably weaker, with amplitudes of $\sim 25\,\mathrm{pc}$ and $\sim 1\,\mathrm{km\,s^{-1}}$, respectively. The bends in the unwarped model also reach far inside the disc reaching the very centre. At first sight, the structure of the bends in both models does not appear to have any distinct shape and wavelength, requiring a more in-depth spectral analysis of the surface $\langle z \rangle$ distributions to probe for bending waves.

4.2 Spectral analysis of bending waves

Bending waves propagating in a kinematically cool galactic disc can be seen as the superposition of a 'fast' (+) and 'slow' (-) waves circulating with frequencies $\omega = m\Omega(R) \pm \nu(R)$, where $\Omega(R)$ is the angular rotation curve, $\nu(R)$ is the vertical frequency, and m-fold rotational symmetry is assumed. The inclusion of the disc's self-gravity raises $\nu(R)$, making bending waves more stable, i.e. stiffer (contrary to density waves) – see Binney & Tremaine (2008). The detailed inclusion of the disc's self-gravity, however, defies simple theoretical modelling, since it depends on the mass distribution of the bending wave itself. Moreover, the halo strongly reacts to the perturbed disc (Binney et al. 1998), making it impossible to model an equation of motion for the disc alone.

We are thus left with the conservative constraint that ignores self-gravity and, for a given rotation curve $\Omega(R)$, bending waves can only propagate in regions that satisfy the condition

$$m^2 \left[\Omega_{\rm p} - \Omega(R) \right]^2 \ge \nu_{\rm h}^2,\tag{1}$$

where $\Omega_{\rm p}=\omega/m$ is the pattern speed and $\nu_{\rm h}$ is the frequency of vertical oscillation contributed by the halo potential. This defines, for m=1, a 'forbidden' region, $\Omega-\nu_{\rm h}<\Omega_{\rm p}<\Omega+\nu_{\rm h}$, where bending waves cannot propagate (e.g. Nelson & Tremaine 1995).

In flattened potentials, $\nu > \Omega$, so the 'fast' wave is prograde, with a frequency ω depending strongly on R for most radii, so differential rotation winds it up rapidly and it decays. The 'slow' wave, on the other hand, is retrograde and circulates with frequency only weakly depending on R for most radii. This wave is thus expected to wind up slowly and be long-lived.

In order to investigate in detail the propagation of bending waves in our models, in this section, we employ the spectral analysis technique of Sellwood & Athanassoula (1986), using a code based on that of

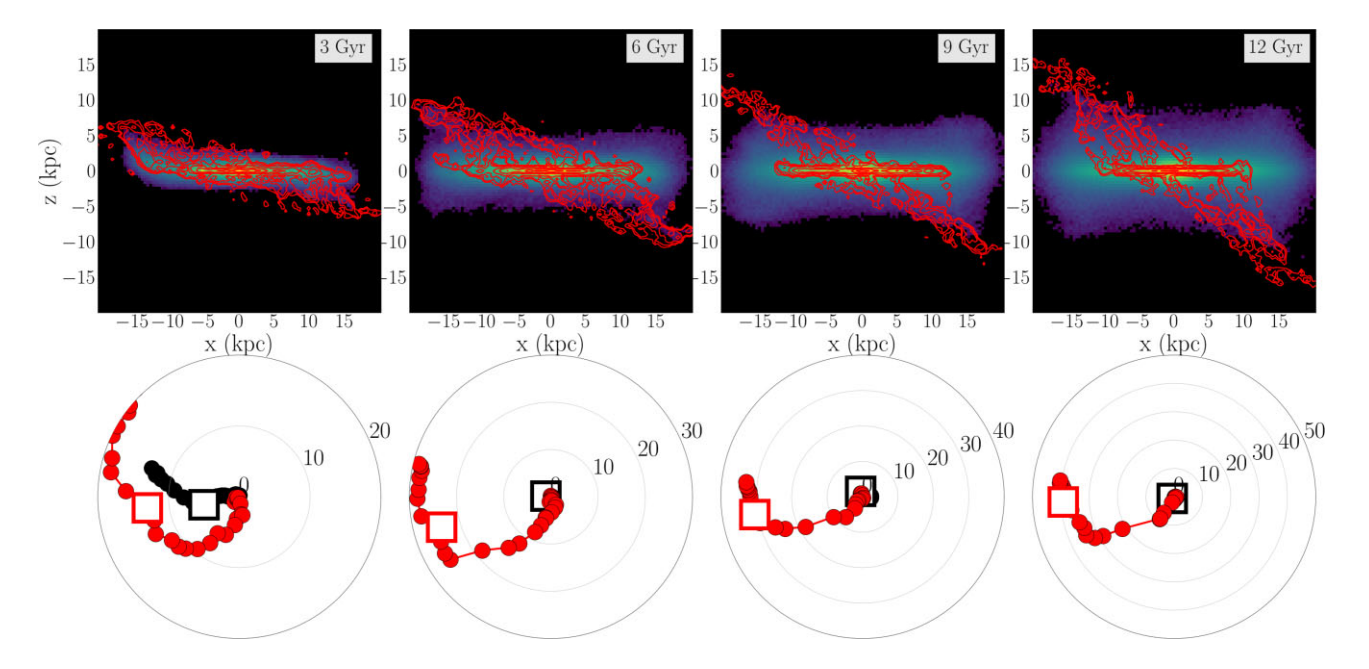


Figure 2. Top row: edge-on views of the stellar and cold gas $(T_{\rm g} \le 50\,000~{\rm K})$ distributions at four times in the evolution of the warped model. The colour represents the stellar surface density, while the red contours represent the cold gas column density. The times are labelled at the top right in each panel. A warp is present throughout the evolution of the warped model. The simulation is rotated so that the major axis of the warp is along the *x*-axis. The warp reaches heights $|z| \sim 15~{\rm kpc}$ over this evolution. Bottom row: Briggs figures for the warped model showing the evolution of the stellar (black) and cool gas (red) warps at the same time. Markers represent annuli with $\Delta R = 0.5~{\rm kpc}$, equally spaced from 5 to 20 kpc, with the square markers indicating $R = 15~{\rm kpc}$. Annuli containing a total mass that is $\le 10^6~{\rm M}_{\odot}$ are not shown. The stellar disc is somewhat warped at $t = 3~{\rm Gyr}$ but becomes flatter throughout its evolution.

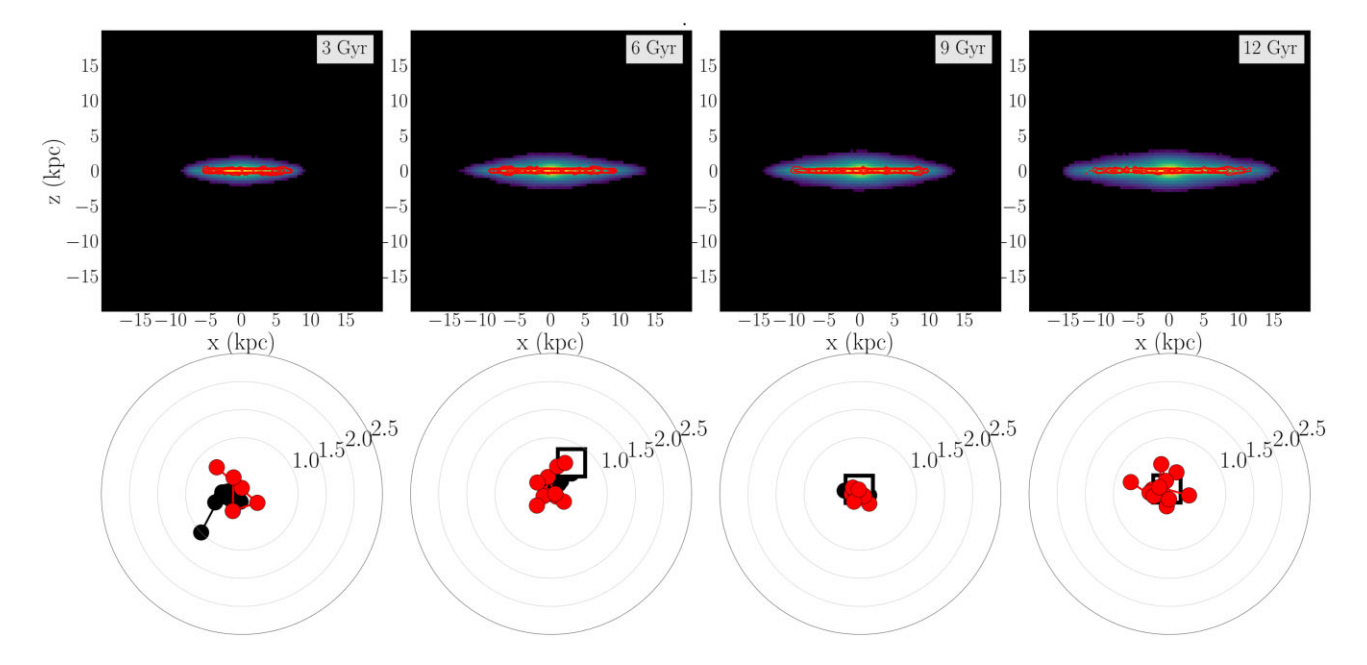


Figure 3. Similar to Fig. 2 but for the unwarped model. In contrast to the warped model, there are no warps in either the gaseous or stellar components in the edge-on distributions. The Briggs figures have a reduced scale with max $\theta = 2.5^{\circ}$ set as the upper limit, so even though we see some changes at different radii, both gas and stellar discs are quite flat throughout the model's evolution.

Roškar et al. (2012). This allows us to recover the spatial distribution and temporal evolution of pattern speeds. The code is applied to both the unwarped and warped simulations, first for the density distribution and then for the vertical distribution.

At each snapshot, we start by selecting star particles in concentric annuli. In each annulus, we first expand the azimuthal angular dependence of the normalized mass distribution in a Fourier series

$$\mu(R,\phi) = 1 + \sum_{m=1}^{\infty} c_m(R) e^{-im\phi},$$
 (2)

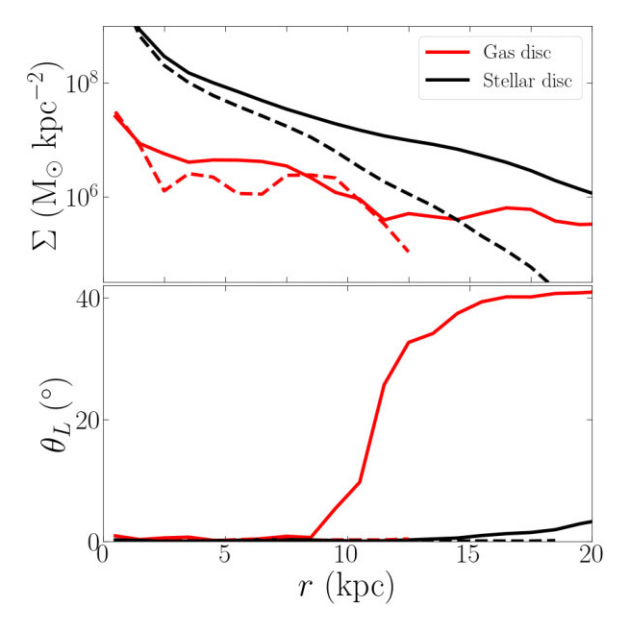


Figure 4. Profiles of the surface density, Σ (top), and $\theta_{\rm L, gas}$ (bottom) in the warped (solid lines) and unwarped (dashed lines) models at t=12 Gyr. The profiles are shown for both the cold gas (red) and stellar (black) discs. Only bins containing a total mass $\geq 7 \times 10^6$ M_{\odot} are shown.

with

$$c_m(R) = \frac{1}{M(R)} \sum_{p=1}^{N} m_p e^{im\phi_p},$$
 (3)

where the sum runs over particles inside the annulus, m_p and ϕ_p are the mass and azimuth of particle p, respectively, and M(R) is the total mass within the annulus. We calculate the coefficients $c_m(R)$ for every snapshot in a given time interval (hereafter baseline) and then perform a discrete Fourier transform of this time series as

$$C_{m,k}(R) = \sum_{j=0}^{S-1} c_m(R, t_j) w_j e^{-2\pi i j k/S},$$
(4)

with k = -S/2,..., S/2, where S is the number of snapshots in the baseline. The associated frequencies are given by

$$\Omega_k = \frac{2\pi}{m} \frac{k}{S\Delta t},\tag{5}$$

where Δt is the time between snapshots, and we adopt the Gaussian window function

$$w(j) = e^{-(j-S/2)^2/(S/4)^2}. (6)$$

Finally, the power spectrum is computed as

$$P(R, \Omega_k) = \frac{1}{W} |C_{m,k}(R)|^2, \tag{7}$$

where

$$W = S \sum_{j=0}^{S-1} w_j^2. (8)$$

We perform this calculation for a time baseline $S\Delta t = 1$ Gyr, resulting in a resolution $\Delta\Omega = 2\pi/m \text{ km s}^{-1} \text{ kpc}^{-1}$ – see equation (5). We repeat this calculation for several time baselines, and the resulting power spectrum for the unwarped simulation is shown in Fig. 6.

In order to analyse the bending signal, similarly to equation (3) we define

$$\gamma_m(R) = \frac{1}{M(R)} \sum_{p=1}^{N} z_p m_p e^{im\phi_p},$$
(9)

where z_p is the vertical height of particle p, and we use equations (4)–(7) mutatis mutandis. Note that now $\gamma_m(R)$ is given in kpc and the associated power spectrum is given in kpc².

Finally, after calculating the power spectra, equation (7), for both density and bending signals, we identify the pattern speeds Ω_p as peaks in the radially integrated power spectra, which we refer to as total power. However, while the disc surface density decreases exponentially with radius, the Fourier coefficients, equations (3) and (9), are normalized by the annulus total mass M(R), giving 'equal weights' to power at small or large radii. Thus, to better appreciate the relevance of different pattern speeds to the disc dynamics, the total power is weighted by the annulus mass:

total power(
$$\Omega_k$$
) = $\frac{\sum M^2(R)P(R,\Omega_k)}{\sum M^2(R)}$, (10)

with the sum running over radial bins. This total power is shown as curves next to the spectrograms in Fig. 6.

For the analysis in this section, we also compute the frequencies of circular motion $\Omega(R)$ and radial oscillation $\kappa(R)$ produced by the total potential and the frequency of vertical oscillation produced by the halo $\nu_h(R)$, using AGAMA (Vasiliev 2019). These frequencies are computed in the middle of each 1 Gyr baseline.

4.2.1 Unwarped simulation

The two left-hand columns of Fig. 6 show, for the unwarped simulation, the power spectra obtained for m=1 and 2 density perturbations (as indicated in the titles) in the (Ω, R) plane at different times (rows), from 5 to 12 Gyr. The m=2 density signal shows multiple pattern speeds at all times, covering a large radial extent and revealing the presence of multiple spiral density waves. The thick dashed white lines show the rotation curves, $\Omega(R)$, while the thin dashed white lines represent $\Omega \pm \kappa/m$.

The panels at the right of the spectrograms show the (massweighted) total power (light and dark red), equation (10) (on a log scale), whose peaks reveal the pattern speeds; prominent peaks for m=2 are immediately distinguished. In an iterative scheme similar to that of Roškar et al. (2012), we identify the most prominent peak, fit a Gaussian function to it, and subtract this Gaussian contribution from the total power. Then, we identify the next most prominent peak and repeat the process, identifying pattern speeds and power in the interval $-100 \le \Omega / \text{km s}^{-1} \text{ kpc}^{-1} \le 100 \text{ up to a maximum of}$ four peaks (horizontal lines, with length representing the power after the Gaussian subtraction of peaks previously identified). The m=1density signal shows some significant power, but the peaks are not as prominent as those for m = 2. It is interesting to note a prominent m =2 retrograde peak at the final baseline (bottom row), with power in the very inner disc. We verified that this is associated with a tiny bar that must have a prograde rotation so fast that the algorithm misinterprets it as a retrograde motion, given the simulation cadence. This peak is enhanced by the mass-weighted normalization of the total power, equation (10), but it is not of interest for our results.

Fig. 7 (left-hand panels) shows the identified m = 1 (top) and 2 (bottom) density pattern speeds for several 1 Gyr baselines, with colours representing the total power for a given pattern speed (Fig. 6). Focusing on m = 2, this figure clearly shows the simultaneous

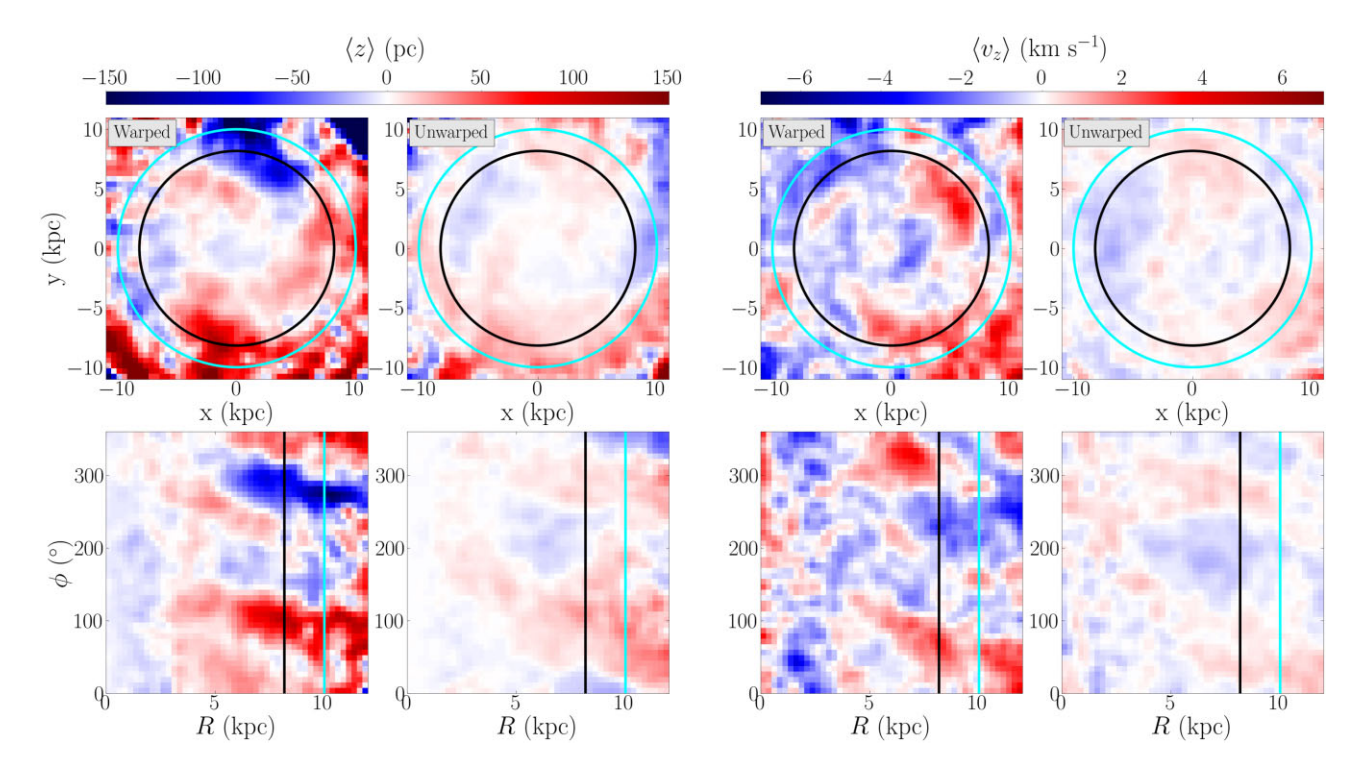


Figure 5. Distributions of the stellar mean height, $\langle z \rangle$ (left), and mean vertical velocity, $\langle v_z \rangle$ (right), for the warped and unwarped simulations (see top left annotation) at t=11.7 Gyr in the x-y (top) and $R-\phi_w$ (bottom) planes. The sense of rotation is clockwise (top row) and towards increasing ϕ (bottom row). A Gaussian filter has been applied to the colour distribution in each panel with a standard deviation of the Gaussian kernel set to $\sigma=1$ pixel = $450\,\mathrm{pc}\times450\,\mathrm{pc}$ (top) and $\sigma=1$ pixel = $250\,\mathrm{pc}\times7.5^\circ$ (bottom). The solid black and cyan circles (vertical lines) represent the solar annulus, $R=8.18\,\mathrm{kpc}$, and $R=10\,\mathrm{kpc}$, in the x-y ($R-\phi$) plane, respectively.

presence of multiple pattern speeds. The higher pattern speeds, at $60\text{--}75\,\mathrm{km\,s^{-1}\,kpc^{-1}}$, decreasing in time are due to the presence of a slowing bar (see Fiteni et al. 2021). The other two prominent pattern speeds can be attributed to the propagation of spiral density waves. In this simulation, for the time interval analysed, the pattern speeds show some evolution, changing values and power amplitude, but not very vigorously transient behaviour. The most prominent patterns are at $\Omega \approx 20\text{--}25$ and $40\,\mathrm{km\,s^{-1}\,kpc^{-1}}$. As shown in Roškar et al. (2012), what is transient about these spirals is not necessarily their frequency, with some values seemingly preferred, but their amplitude, which continuously varies. We cannot exclude the possibility that certain modes are continuously being re-excited, most likely with random relative phases.

The power spectra for the m=1 and 2 bending signal in the unwarped simulation are shown in the two right-hand columns of Fig. 6 (see the titles). The panels to the right of these spectrograms again show the (mass-weighted) radially integrated power spectra (dark and light blue) with the peaks identified in the same way as before. The white thick dashed lines again show the rotation curve $\Omega(R)$, while the shaded white areas between $\Omega \pm \nu_h/m$ represent the forbidden regions for bending waves – equation (1). Focusing on m=1, the most noticeable feature in these spectra is the ubiquitous presence of a slow retrograde pattern at $-15 \lesssim \Omega/\,\mathrm{km\,s^{-1}\,kpc^{-1}} \lesssim -10$ and extending inwards to $R \approx 5\,\mathrm{kpc}$, where $\Omega - \nu_h$ (bottom thin dashed curves) starts to strongly depend on R and severe winding is expected for kinematic bending waves.

The right-hand panels of Fig. 7 show the evolution of the pattern speeds identified for the bending signals of m=1 (top) and m=2 (bottom) multiplicity. Focusing again on m=1, we confirm the ubiquitous presence of the slow retrograde mode, while prograde

bending waves are barely noticeable. This seems in accordance with the theoretical expectation that, no matter how the bending perturbation is produced, the associated slow retrograde wave is long-lived, while prograde waves, if present, decay quickly. Interestingly, a prograde m=1 bending pattern, at $\Omega\approx 20-25\,\mathrm{km\,s^{-1}\,kpc^{-1}}$, is detected at some snapshots, located inside the forbidden region for bending waves, but with very small power (see Fig. 6).

4.2.2 Warped simulation

Fig. 8 shows the power spectra for the warped simulation (in this simulation, we stored outputs at high cadence already from 2 Gyr, which permits us to perform spectral analysis from this point onwards), with the same scheme of density and bending m=1 and 2 signals as in Fig. 6. As in the unwarped model, the m=2 density signal exhibits multiple pattern speeds present simultaneously, covering a large radial extent. The pattern speeds are not as sharply defined as in the unwarped simulation, which might be due to the perturbation from the warp. Alternatively, this could be due to the warped model being thicker: At 12 Gyr and between $5 \le R/\text{kpc} \le 10$, the discs of the warped and unwarped models have root mean square (RMS) z, of 0.94 and 0.55 kpc, respectively. The left-hand panels of Fig. 9 show the time evolution of the pattern speeds identified in Fig. 8 for the m=1 (top) and m=2 (bottom) density signal. Note that no bar forms in this simulation.

The right-hand panels of Fig. 8 show the spectrograms for the bending signals. The bending m=1 waves exhibit a prominent peak at $\Omega = 0 \,\mathrm{km}\,\mathrm{s}^{-1}\,\mathrm{kpc}^{-1}$ for almost all snapshots, which is the trivial signal of the warp itself. This peak is so prominent that it can visually hide nearby peaks, which our iterative peak finding

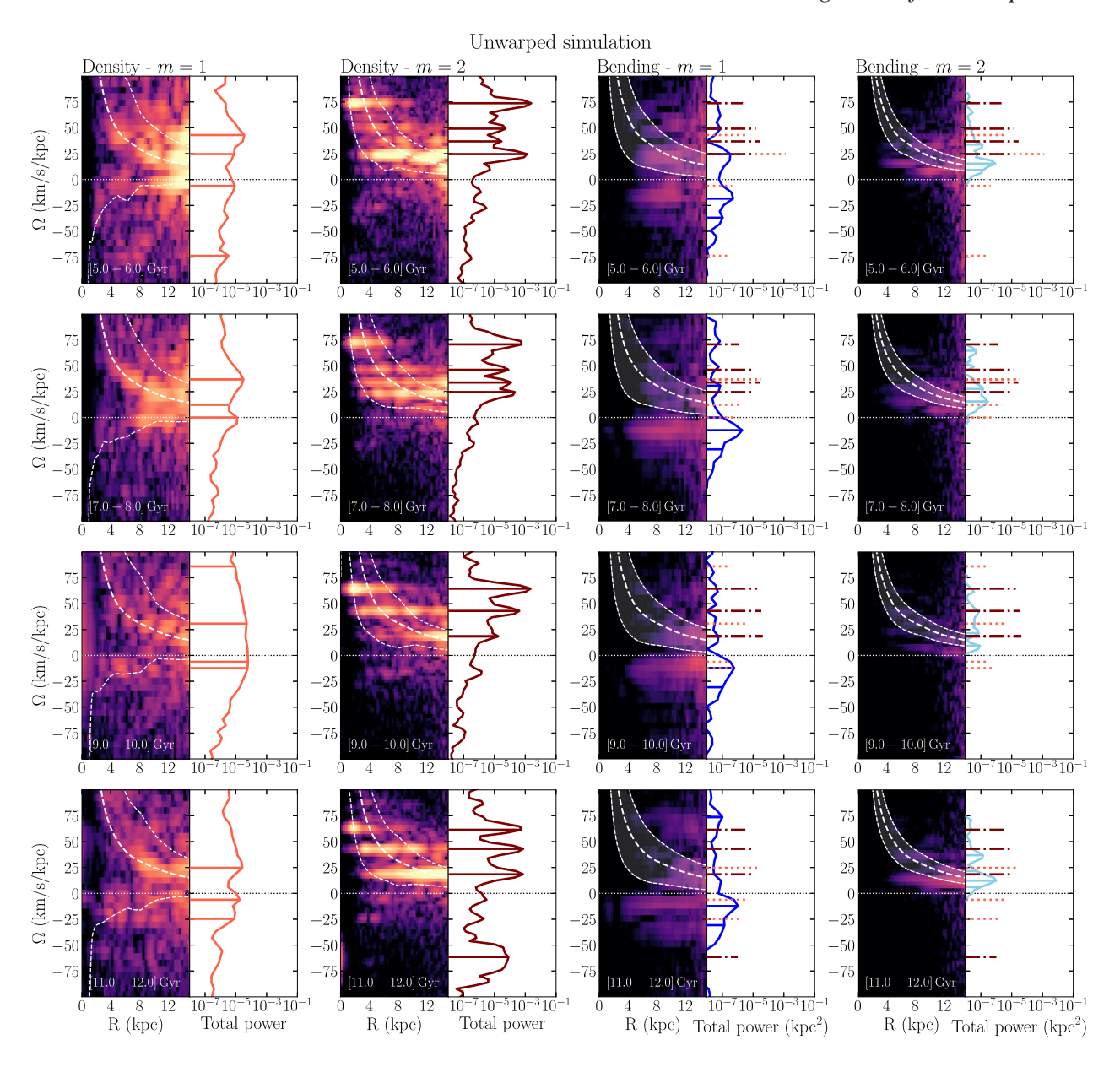


Figure 6. Power spectra for perturbations in the unwarped simulation at several time intervals (rows). The first two columns show the power spectra for m=1 and 2 density (bar + spiral) perturbations, with the mass-weighted radius-integrated power shown to the right of the spectrograms – see equation (10). The thick and thin white dashed lines show $\Omega(R)$ and $\Omega \pm \kappa/m$, respectively. The two right-hand columns show the power spectra for m=1 and 2 bending perturbations. The thick and thin white dashed lines show $\Omega(R)$ and $\Omega \pm \nu_h/m$, respectively, and the white shaded areas between these curves represent the forbidden regions for bending waves. For m=1, the expected long-lived slow retrograde motion is clearly visible, while the fast prograde pattern is weak. The total power peaks of the m=1 (light red dotted lines) and m=2 (dark red dot-dashed lines) density perturbations are repeated in the two right-hand columns.

and Gaussian subtraction scheme allows us to detect (dark blue horizontal lines). The m=1 peak due to the slow retrograde motion $(\Omega \approx -15 \,\mathrm{km \, s^{-1} \, kpc^{-1}})$ is detected at almost all time intervals. Additionally, significant power in fast prograde waves is now observed, at large radii, and peaking at $25 \leq \Omega / \mathrm{km \, s^{-1} \, kpc^{-1}} \leq 50$.

The time evolution of the pattern speeds identified in Fig. 8 for the m=1 (top) and m=2 (bottom) bending signals is presented in the right-hand panels of Fig. 9. As in the unwarped simulation (Fig. 7), we see the ubiquitous presence of a slow, retrograde m=1 wave in the warped simulation, with substantially more power than in that model.

The main difference between the warped and unwarped models is the presence of a strong, fast prograde motion in the m=

1 bending signal, at $25 \lesssim \Omega/\,\mathrm{km\,s^{-1}\,kpc^{-1}} \lesssim 50$ in the warped system. These fast prograde patterns peak at large radii (see Fig. 8), thus avoiding the forbidden region for bending waves. Note that the prograde bending waves are present at all times. This is due to the long-lived nature of the warp in this simulation. While fast prograde bending waves are expected to decay quickly, the warp continuously perturbs the disc, re-exciting these waves.

The main conclusion from the analysis in this section is that slow retrograde bending waves are present in both the unwarped and warped models, throughout their evolution. On the other hand, only in the warped model are significant fast prograde bending waves detected, which must be persistently re-excited by the warp.

Unwarped simulation Total power Total power (kpc²) 75 75 50 50 H $\Omega \; (\mathrm{km/s/kpc})$ -50 10^{-4} -75<u>1</u>2 t (Gyr)t (Gyr)Density - m=2Bending - m=275 10^{-5} 50 50 25 -25-25-50-50 75

Figure 7. Pattern speeds in the unwarped model identified in Fig. 6, for m=1 (top) and m=2 (bottom) density (left) and bending signals (right). Colours indicate the mass-weighted radially integrated power. Different colour scales are chosen to differentiate between the density and bending pattern speeds. For the m=2 density signal, the gradual decrease of the highest pattern speed (upper points) is suggestive of a slowing bar (see the centre-left column of Fig. 6). The other two discernible patterns are associated with spiral density waves, with the most prominent ones at $\Omega \approx 20$ –25 and $40 \,\mathrm{km} \,\mathrm{s}^{-1} \,\mathrm{kpc}^{-1}$. The m=1 bending plot shows the long-lived presence of a slow retrograde pattern (at $-15 \le \Omega/\,\mathrm{km} \,\mathrm{s}^{-1} \,\mathrm{kpc}^{-1} \le -10$) and (at some times) a very weak prograde signal at $\Omega \approx 24 \,\mathrm{km} \,\mathrm{s}^{-1} \,\mathrm{kpc}^{-1}$.

4.3 The source of the vertical perturbations

5

6

In the previous section, we demonstrated the presence of bending waves in both the warped and unwarped simulations, with different properties. Bending waves in simulations of unwarped isolated galaxies were already reported by Chequers & Widrow (2017), who suggested shot noise in the dark matter halo as a source mechanism. Fast prograde bending waves are expected to dissipate rapidly and therefore be weak, as indeed we find in the unwarped simulation. However, in the warped model the consistent power in the prograde bending waves indicates that the disc in the warped model is continuously being vertically excited.

 $t \, (Gvr)$

10

11

12

We now verify that the gas inflow along the warp is the source of these vertical perturbations. We start from the continuity equation:

$$\frac{\partial \rho}{\partial t} + \nabla \cdot (\rho \mathbf{u}) = 0, \tag{11}$$

where ρ and \mathbf{u} are the density and velocity of the gas at a certain location, respectively. Integrating over a spherical volume of radius R,

$$\frac{\mathrm{d}M}{\mathrm{d}t} = - \oiint \rho \mathbf{u} \cdot \mathrm{d}\mathbf{S},\tag{12}$$

where M is the total gas mass inside the volume and the last integral is evaluated on the enclosing spherical surface, with $dS = R \sin \theta \ d\theta \ d\varphi$. The flux can be measured in two different

ways: (i) as $(1/4\pi R^2) \delta M/\delta t$, i.e. using the difference, between two snapshots, of the total gas mass inside the sphere (thus averaging over δt); or (ii) estimating the integral on the right-hand side of equation (12) in a shell of small but finite thickness δR (thus averaging over δR). The first method presents practical problems because, at the centre of the volume, a fraction of gas will form stars. Moreover, we are interested in the gas *inflow* along the warp, as opposed to total mass variation, which includes feedback-driven outflows. Finally, we are interested in the frequencies associated with the variation of the gas flux; thus, we opt to use single snapshots at each time, i.e. the second method.

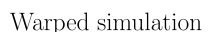
10

t (Gvr)

We compute the right-hand side of equation (12) via a Monte Carlo integration. For this, we introduce the function f, which represents the underlying probability distribution from which particles in the shell are sampled, such that $\int f \, dS = 1$. The right-hand side of equation (12) is estimated as

$$I \equiv - \oiint \frac{\rho \mathbf{u}}{f} f \cdot d\mathbf{S} \approx -\frac{1}{N} \sum_{i} \frac{\rho_{i} u_{ri}}{f_{i}}, \tag{13}$$

where we sum over gas particles in the shell (N particles), ρ_i is the density around particle i, u_{ri} is its radial velocity component, and we select cool gas ($T_g \le 50\,000\,\mathrm{K}$) particles with $u_{ri} < 0$. The sampling function f is obtained marginalizing over the number density profile,



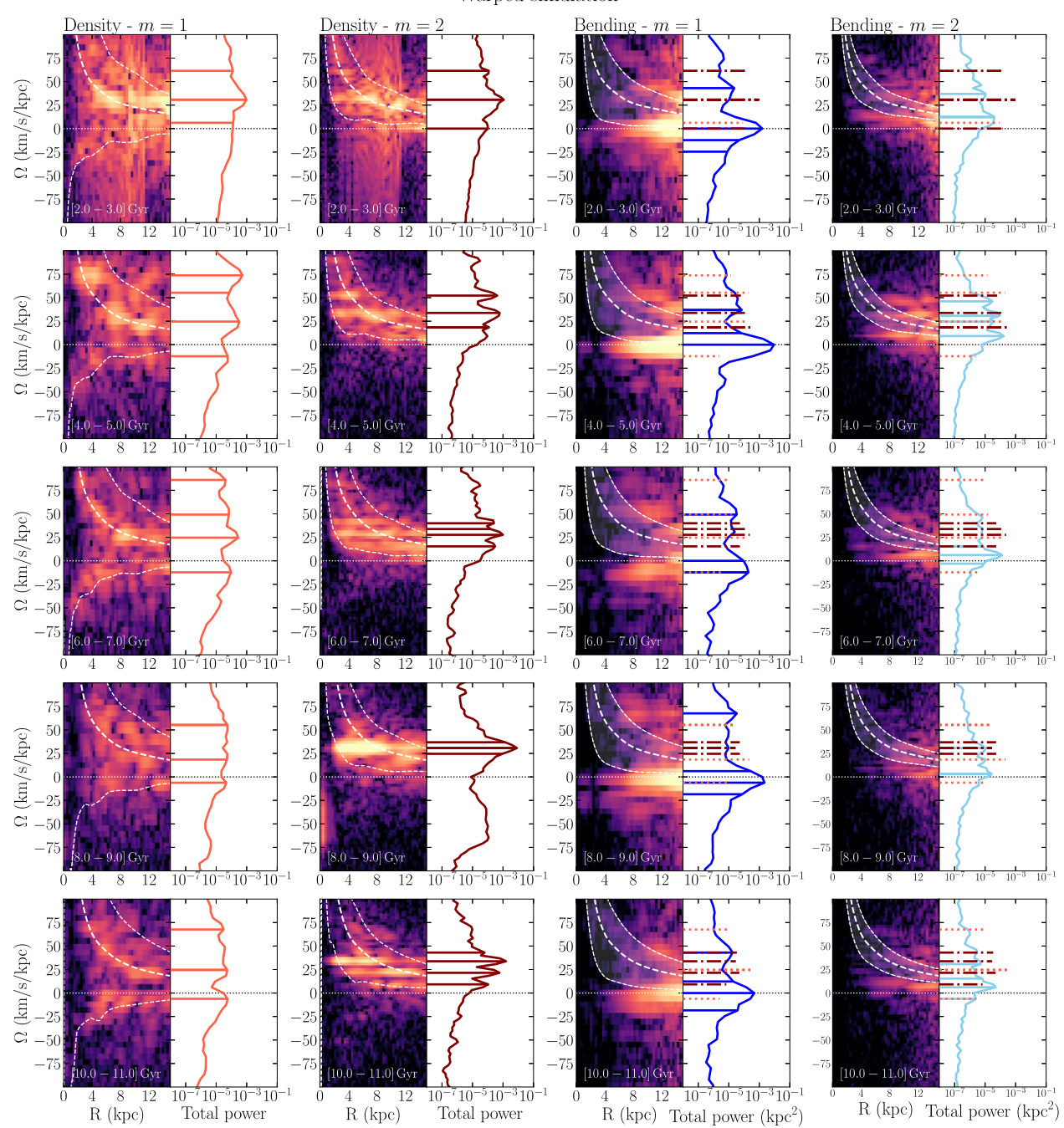


Figure 8. Similar to Fig. 6, showing the power spectra at different times (rows) for the m=1 and 2 density (left) and bending (right) perturbations in the warped simulation. The m=2 density panels show the simultaneous presence of various pattern speeds between the Lindblad resonances. In the m=1 bending panels, the most noticeable difference with respect to Fig. 6 is the strong peak at $\Omega \approx 0 \,\mathrm{km}\,\mathrm{s}^{-1}\,\mathrm{kpc}^{-1}$, which is a trivial manifestation of the warp. As in the unwarped simulation, a slow retrograde motion is detected in the m=1 bending plot. Significant m=1 bending power is present for large Ω at large radii, i.e. a fast prograde motion avoiding the forbidden region for bending waves, and peaking at $25 \leq \Omega/\mathrm{km}\,\mathrm{s}^{-1}\,\mathrm{kpc}^{-1} \leq 50$.

 $n(R, \theta, \varphi)$, within the shell,

$$f(\theta, \varphi | R) = \frac{1}{N} \int_{R - \delta R/2}^{R + \delta R/2} n(R', \theta, \varphi) \, \mathrm{d}R' \approx \frac{1}{N} n(R, \theta, \varphi) \delta R. \quad (14)$$

Substituting into equation (13), we finally estimate the flux as

$$\frac{I}{4\pi R^2} \approx -\frac{1}{4\pi R^2 \delta R} \sum_{i} m_i u_{ri},\tag{15}$$

where m_i is the mass of particle i and we approximated the density around the particle by the smooth density profile evaluated at the centre of the shell, i.e. $\rho_i \approx \rho(R, \theta, \varphi)$.

The top panel of Fig. 10 shows the evolution of the inward mass flux of cool gas ($T_{\rm g} < 50\,000$ K) through a spherical shell with a thickness $\delta R = 0.2\,{\rm kpc}$ and a radius $R = 15\,{\rm kpc}$. The flux of cool gas varies substantially, with long-term inflow modulated by rapid variations. Similar to the analysis in Section 4.2, we apply a discrete Fourier transform to the evolution of the mass flux over 1 Gyr

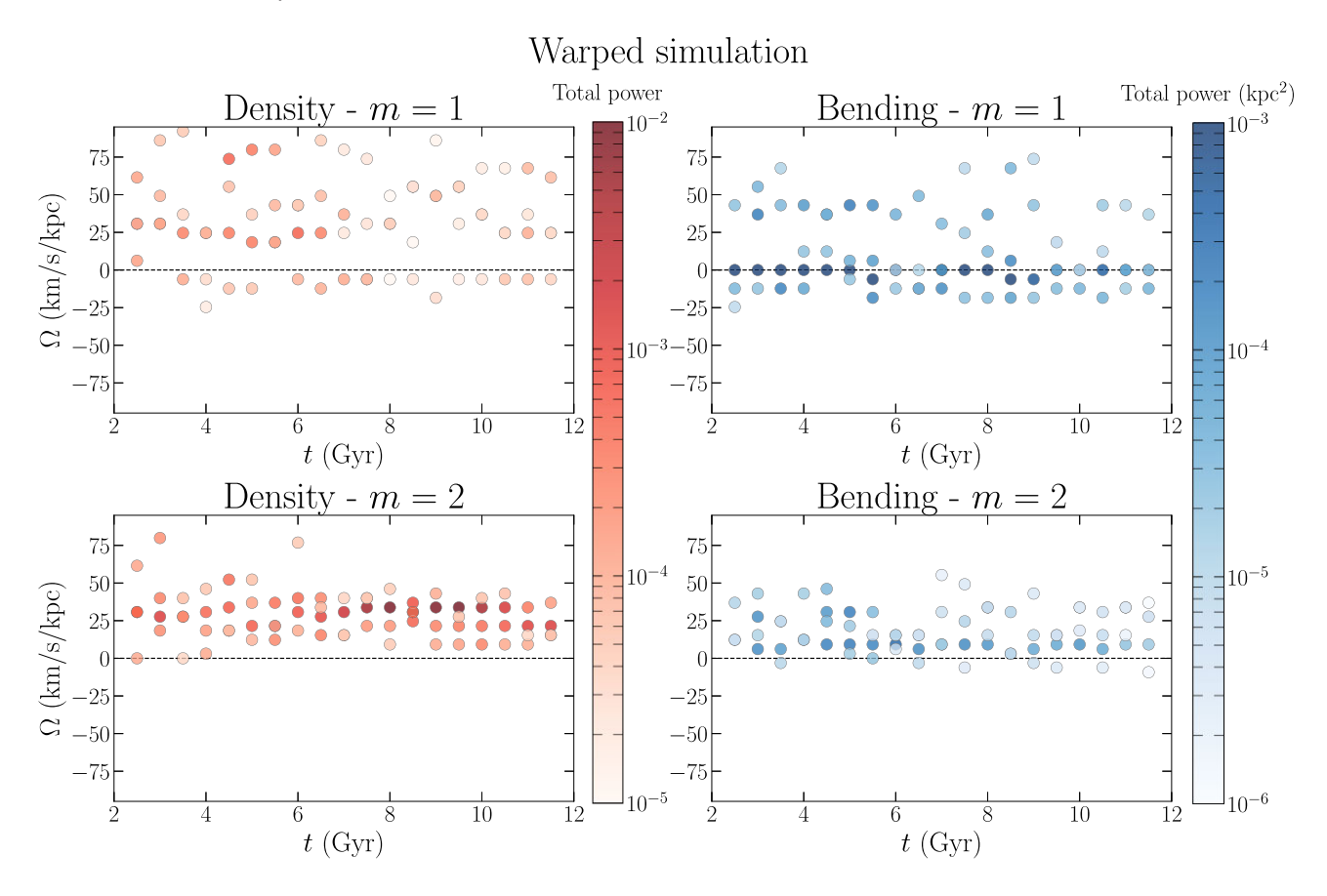


Figure 9. Evolution of the pattern speeds identified in Fig. 8, for the warped simulation. The m=2 density panel reveals a more transient evolution, in comparison to the unwarped simulation. In the m=1 bending panel, the darkest points (power $\gg 10^{-4} \, \mathrm{kpc^2}$) lying at $\Omega \approx 0 \, \mathrm{km \, s^{-1} \, kpc^{-1}}$ represent a trivial manifestation of the warp. As in the unwarped simulation (Fig. 7), a persistent slow retrograde m=1 bending signal is detected. Unlike the unwarped simulation, a fast m=1 bending prograde motion ($25 \le \Omega / \mathrm{km \, s^{-1} \, kpc^{-1}} \le 50$) is detected with substantial power.

baselines to derive the characteristic time-scales of the variations. The bottom panel of Fig. 10 shows the resulting frequencies of the mass flux. Most of the frequencies cluster between 0 and 20 kpc km s $^{-1}$, and reach to 40 kpc km s $^{-1}$. These results show that the disc is continuously perturbed by the irregularly accreting gas with a maximum amplitude of $5.8\times10^6\,M_\odot\,kpc^{-2}\,Gyr^{-1}$, and typical amplitudes of $\sim\!10^6\,M_\odot\,kpc^{-2}\,Gyr^{-1}$, which is comparable to recent estimates of the gas inflow in the MW (Fox et al. 2019; Werk et al. 2019). These frequencies substantially overlap the frequencies of the bending waves, indicating a favourable spectrum of perturbations for exciting the bending waves. We therefore propose that the irregular inflow of gas from the warp on to the disc is the source of the vertical perturbations that excite the bending waves in the warped model.

To further demonstrate that cold gas accretion has direct impact on the vertical structure of the galactic disc, we analyse the evolution of the gas flux relative to the total vertical power at different annuli. We estimate the total vertical power by calculating $\langle z \rangle$ in sectoral non-overlapping bins with $\Delta \phi_w = 12^\circ$ at each annulus and then taking the RMS across the azimuthal bins.

Fig. 11 shows the evolution of the flux (black) and RMS($\langle z \rangle$) (red) at the solar annulus (dotted) and the outskirts of the disc (solid). Measuring the cross-correlation between the flux and RMS($\langle z \rangle$) shows that there is a lag of \sim 200 and \sim 250 Myr at the outer disc and solar annulus, respectively. The overall lag is expected as the gas flux is measured at R=15 kpc, so it takes time to reach and impact the disc. The \sim 50 Myr lag between peak in the outer disc and that at

the solar annulus represents the time required for the excited waves to propagate from the outskirts to the solar annulus. Considering the distance $\Delta R \sim 1.8$ kpc, this signal propagates with a velocity of ~ -36 pc Myr⁻¹ (the minus sign indicating inward propagation).

We can now link this velocity with the expected group velocity of bending waves, $d\omega/dk$. For a simple estimate, we use the WKB dispersion relation for an m = 1 bending wave (Toomre 1983)

$$[\omega - \Omega(R)]^2 - 2\pi G \Sigma(R)|k| - v_h^2 = 0, \tag{16}$$

where k is the wavenumber and $\Sigma(R)$ is the surface density. The expected group velocity is then

$$\frac{\mathrm{d}\omega}{\mathrm{d}k}\bigg|_{R} = \frac{\mathrm{sgn}(k)\pi G\Sigma(R)}{\Omega_{\mathrm{p}} - \Omega(R)},\tag{17}$$

according to which a negative group velocity can be associated with a leading (k < 0) prograde wave or to a trailing (k > 0) retrograde wave. The spectral analysis showed an overall larger power in the retrograde wave, and Fig. 5 suggests a trailing shape. Substituting the value $\Omega_{\rm p} = -12.8~{\rm km\,s^{-1}\,kpc^{-1}}$ identified in Fig. 9 at late times, and $\Sigma = 80\,{\rm M}_{\odot}\,{\rm pc^{-2}}$ and $\Omega = 18.6\,{\rm km\,s^{-1}\,kpc^{-1}}$ (values at $R \sim 9.1\,{\rm kpc}$), we obtain a radial group velocity of $\sim -35\,{\rm pc\,Myr^{-1}}$, in striking agreement with the value obtained from the measured time lag. This agreement is somehow surprising given all the approximations and simplifying assumptions involved, so it should be considered with caution.

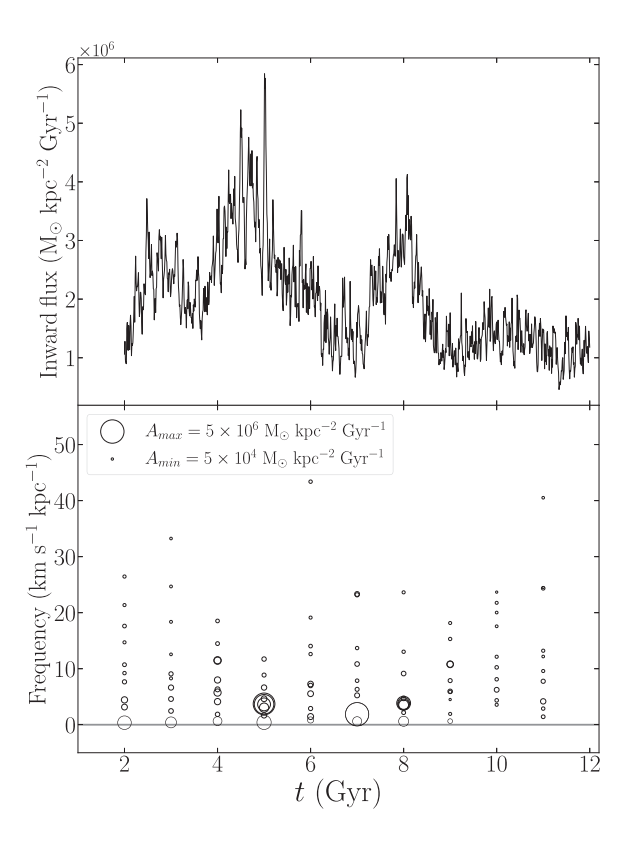


Figure 10. Top: evolution of the inward mass flux of cold gas ($T < 50\,000\,\mathrm{K}$) through a spherical shell with $R = 15\,\mathrm{kpc}$ and $\delta R = 0.2\,\mathrm{kpc}$. Bottom: frequencies derived from a discrete Fourier transform of the mass flux on 1 Gyr baselines. The marker size indicates the amplitude with the values of the maximum and minimum amplitudes and their respective marker sizes shown in the legend.

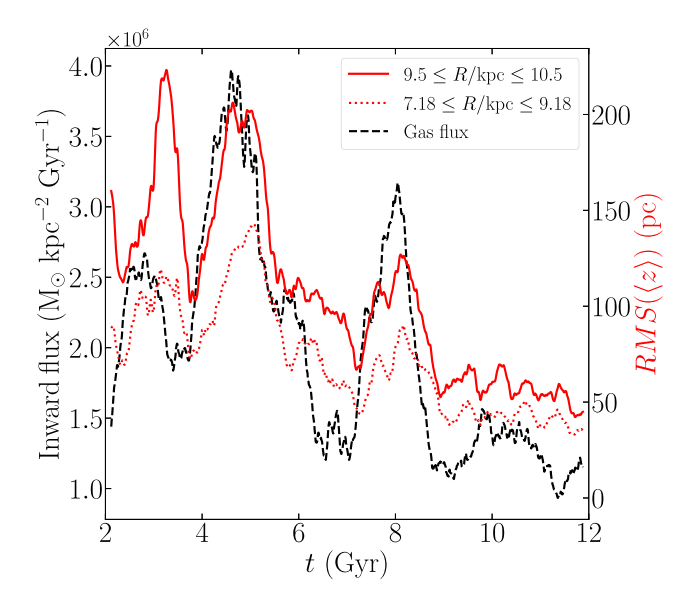


Figure 11. Evolution of the gas flux presented in Fig. 10 (black, left y-axis) and of the RMS of the mean vertical displacement, RMS($\langle z \rangle$) (red, right y-axis), at $7.18 \le R/\,\mathrm{kpc} \le 9.18$ (solar annulus, dotted) and $9.5 \le R/\,\mathrm{kpc} \le 10.5$ (outer disc, solid). RMS($\langle z \rangle$) is calculated using the azimuthally binned $\langle z \rangle$ values in Figs 17 (left column) and 18 (top panel) for the outer disc and solar annulus, respectively. The gas flux and RMS($\langle z \rangle$) are averaged over 0.25 Myr intervals. A cross-correlation analysis of these different series reveals time lags, compared to the gas flux, of 200 and 250 Myr at the outer and inner annuli, respectively (see the main text for details).

4.4 Vertical kinematics in the SN

In Fig. 5, the vertical bends are accompanied by non-zero $\langle v_z \rangle$. SD18 and H18 observed an increase in $\langle v_z \rangle$ with angular momentum $|L_z|$, which they speculated was due to either an extension of the warp or to a bending wave. We test whether such signals arise in our models.

Fig. 12 examines a simulated SN sample in the warped model at 11.4 Gyr, with plots similar to those of SD18 and H18. Three panels plot $\langle v_z \rangle$ versus L_z (top right), versus azimuthal velocity, v_{ϕ} (bottom right), and versus cylindrical and guiding radii, R and $R_{\rm g}$ (bottom left, the latter computed using AGAMA; Vasiliev 2019), respectively. With the improved mapping of the MW's warp, the Sun's position relative to it is now clearer: the Sun is $\sim 17.5 \pm 1^{\circ}$ behind the ascending node of the warp (Chen et al. 2019). Our sample is contained within a sphere of radius 2 kpc at R = 8.18 kpc and azimuth $\phi_w = -17.5^\circ$, where ϕ_w is the azimuthal angle along the direction of rotation measured from ascending node of the warp's LON. The location of our sample is indicated in the top left panel of Fig. 12, on top of a face-on map of $\langle v_z \rangle$. Although all of the binned $\langle v_z \rangle$ variations have relatively larger errors (despite our bins being large compared with SD18 and H18), we observe a general increase of $\langle v_z \rangle$ with $-L_z$ along with underlying wiggles, as in the MW. Following SD18, we fit a variety of functions to the $\langle v_z \rangle$ versus L_7 distribution:

$$\langle v_z \rangle = b + aL_z',\tag{18}$$

$$\langle v_z \rangle = b + aL'_z + A\sin(2\pi L'_z/c + d), \tag{19}$$

and

$$\langle v_z \rangle = b + aL_z' + A\sin(2\pi c/L_z + d), \tag{20}$$

where $L'_z = L_z - 1600 \,\mathrm{kpc} \,\mathrm{km} \,\mathrm{s}^{-1}$ in the MW and a, b, c, d, and A are fitting parameters. For the warped model, we set $L'_z = L_z -$ 2000 kpc km s⁻¹ based on the mean value of L_z at R = 8.18 kpc, but note that in the fit of equation (18) the slope is independent of this pivot point. Assuming v_z is normal distributed and using flat priors for all parameters, we sample the posterior distribution function with the EMCEE package (Foreman-Mackey et al. 2013). The best-fitting parameters for equations (18)–(20) are listed in Table 1 (with uncertainties estimated as the interval containing 68 per cent of samples around the median), and we see that our linear fit is of the same scale as the one measured in the MW. The fits to equations (19)-(20) present larger uncertainties and deviations from the values of SD18 and H18; thus, we mainly focus on the fits of the simple linear function. We also perform linear fits on the other $\langle v_z \rangle$ distributions (versus v_{ϕ} , R, and $R_{\rm g}$), the slopes of which are presented in the bottom right corner of the respective panels. These additional fits are also of the same order as those measured in the SN (SD18; H18).

SD18 argued that one possible interpretation of the non-vanishing slope of the $\langle v_z \rangle$ – L_z relation is that the stellar disc is warped at the solar cylinder. The slope of the relation in this scenario would vary smoothly with azimuth as $\cos{(\phi_w + \phi_c)}$ (where ϕ_c is some constant), which we can check in our model. In Fig. 13, we plot the slope, a, of the linear fit of equation (18) as a function of ϕ_w , the azimuthal angle at which the sample is selected. This relation is plotted for a number of snapshots, with a time interval $\delta t = 20$ Myr to show the short-term changes in the slope. For this measurement, we use 12 samples that consist of 2 kpc spheres. The spheres are equally spaced in azimuth to avoid overlapping the samples. The slope varies in the range of $[-5,5] \times 10^3$ kpc $^{-1}$; SD18 and H18 measure a slope of $\sim 2.64-3.21 \times 10^3$ kpc $^{-1}$, which is within the range we find. The results of these snapshots happen to be instances when the slope at

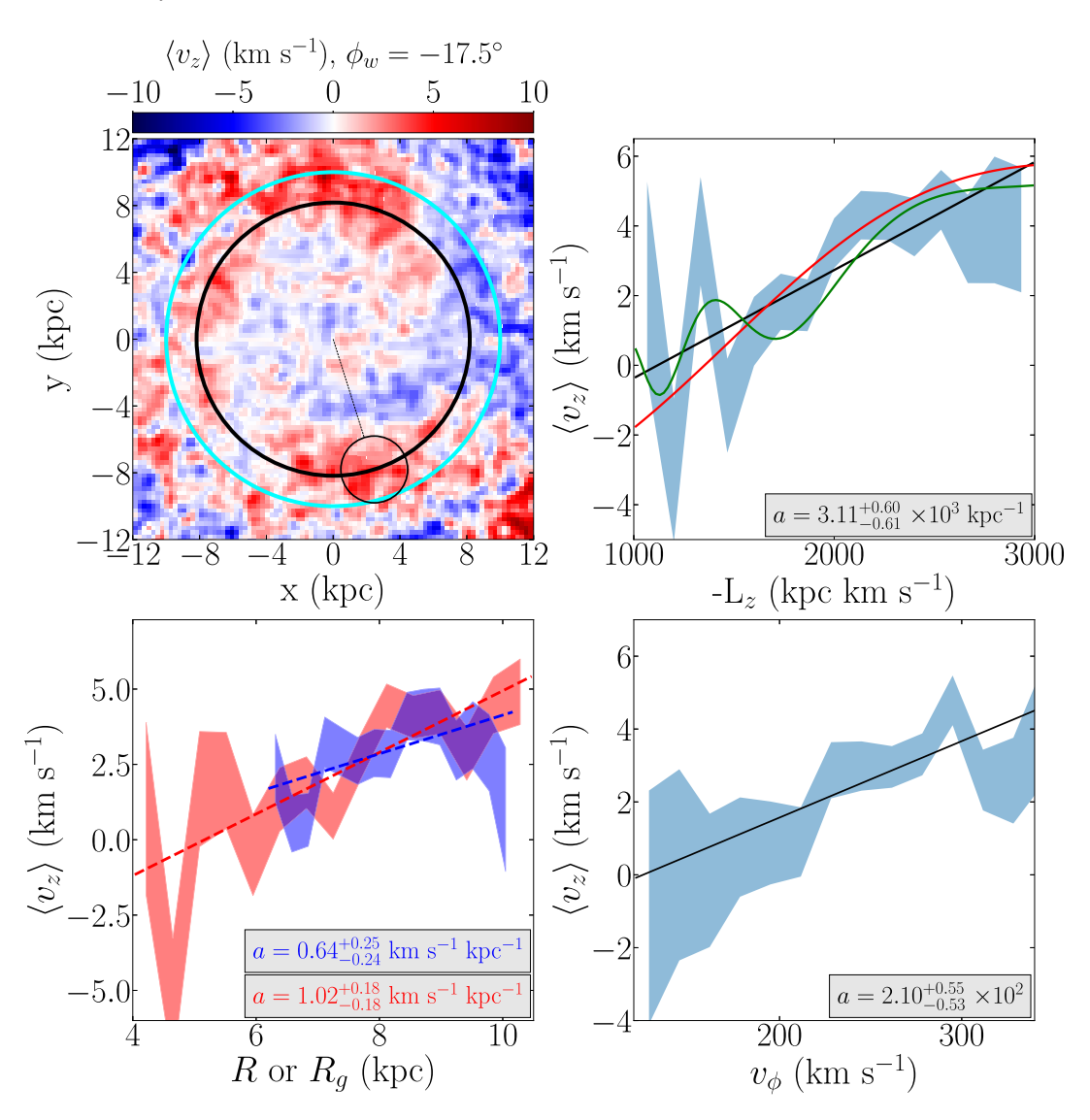


Figure 12. Top left: Distribution of $\langle v_z \rangle$ in the stellar disc of the warped model at 11.4 Gyr. The smaller black circle indicates a region of radius 2 kpc to simulate an SN (azimuth indicated above the colour bar). The larger solid black and cyan circles represent the solar annulus, R = 8.18 and 10 kpc, respectively. A Gaussian filter has been applied to the colour distribution with a standard deviation set to $\sigma = 1$ pixel $= 260 \times 260$ pc. Top right: Binned distribution of $\langle v_z \rangle$ as a function of the angular momentum, L_z , in the SN sample of the warped model. The shaded regions show the standard deviation of $\langle v_z \rangle$ in each bin. There are three model fits present: linear (equation 18, black), sinusoidal (equation 19, red), and wrapping (equation 20, green). The slope of the fitted linear model is shown in the panel's bottom right corner, while the rest of the fit parameters for the linear and other models are presented in Table 1. Bottom left: Binned distributions of $\langle v_z \rangle$ as functions of cylindrical radius, R (blue), and guiding radius, R_g (red), in the same SN sample. Each distribution has a fitted linear model (dashed lines). Bottom right: Binned distribution of $\langle v_z \rangle$ as a function of $\langle v_z \rangle$ as a function of v_{\sigma} in the same SN sample, as well as the fitted linear model. The respective slope values are shown in the bottom right corner of each panel. The choice of time-step is not arbitrary; at 11.4 Gyr is the last moment the SN sample has a slope of $a > 3 \times 10^3$ kpc⁻¹ (see Fig. 16 for details).

Table 1. Best-fitting parameters for the fitting models of equations (18)–(20) applied to the sample in Fig. 12. The slope of the linear fit has been measured in the SN by SD18 ($3.05 \pm 0.25 \times 10^3 \, \text{kpc}^{-1}$) and H18 ($3.11 \pm 0.70 \times 10^3 \, \text{kpc}^{-1}$) that is within the range we find.

Fit	$a \times 10^3 \text{ kpc}^{-1}$	b (km s ⁻¹)	c (kpc km s ⁻¹)	d	$A (\text{km s}^{-1})$
Linear (equation 18)	$3.11^{+0.59}_{-0.58}$	$2.72^{+0.24}_{-0.24}$	_	_	_
Sinusoidal (equation 19)	$2.96^{+0.89}_{-1.4}$	$2.41^{+0.51}_{-5.6}$	$3443.59^{+33459.11}_{-3073.73}$	$0.73^{+1.10}_{-1.72}$	$1.24^{+6.89}_{-0.80}$
Wrapping (equation 20)	$2.72^{+0.66}_{-0.66}$	$2.56^{+0.25}_{-0.25}$	$3601.17^{+151.99}_{-323.90}$	$-2.59^{+1.05}_{-0.42}$	$1.10^{+0.39}_{-0.42}$

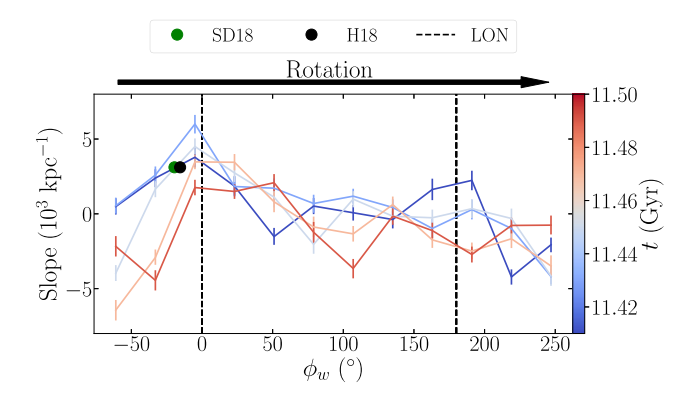


Figure 13. The slope of the $\langle v_z \rangle - L_z$ relation as a function of azimuth for samples at $R=8.18\,\mathrm{kpc}$ in the warped model. The value $\phi_w=0$ is defined as the azimuth on the ascending node of the warp's LON (dashed line). Therefore, the descending node, similarly indicated by a vertical dashed line, is at 180° . The sense of rotation is indicated above the figure. In the MW, the Sun is located 17.5° before the ascending node (Chen et al. 2019), i.e. at $\phi_w=-17.5^\circ$. The black and green dots represent the slope as measured by SD18 and H18, respectively (horizontally offset by $\pm 2^\circ$ for clarity). The panel shows five snapshots separated by 20 Myr. Waves are seen propagating in the direction of rotation, e.g. starting at 50° (dark blue) and reaching 110° (dark red).

the solar azimuth is very similar to that observed in the MW. Note that a varies in a wave-like manner as the peaks and valleys shift with time. As the warp is fixed at each snapshot (see Section 2.3), the positive slope in the $\langle v_z \rangle - L_z$ relation is not produced by the warp itself, but by a propagating bending wave, which suggests that the same may be happening in the MW. The phase of the wave moves in the direction of increasing ϕ_w , i.e. in the sense of rotation.

Fig. 14 plots the variation of $\langle v_z \rangle$ with L_z (top right), v_ϕ (bottom right), and R and R_g (bottom left) in the unwarped model. As the simulation is unwarped, the simulated SN is arbitrary, so we perform our analysis at $R=8.18\,\mathrm{kpc}$ in 30 different azimuths and present the sample with the largest recent slope. The relation is significantly shallower than in the warped simulation. Fig. 15 shows the variation of the slope with azimuthal angle at different times (top panel), similar to Fig. 13. The variation of the slope with azimuth is less pronounced when compared to the warped model and barely reaches the MW values throughout the 2 Gyr interval, with $|a|\lesssim 2\times 10^3\,\mathrm{kpc}^{-1}$. The bottom panel shows the effect of small artificial tilts of the disc about the x (red) and y (blue) axes. These small (0.5°) tilts barely change the slope, indicating that the large slope observed in the MW is not due to a misidentified disc midplane.

Since the unwarped simulation lacks a LON to simulate an SN sample, as in the analysis of Fig. 13, we measure the slope in 12 azimuthally equally spaced 2 kpc spheres. Fig. 16 plots the slope values for these 12 samples (white points) over a 2 Gyr interval starting from t=10 Gyr with $\delta t=10$ Myr. The slope values oscillate about a=0 kpc without reaching the SN values (green dotted line). In contrast, the evolution of the slope in the warped model's SN sample (red solid line) shows strong oscillations about $a\sim0.6\times10^3$ kpc⁻¹ with more than half of the values being positive. There are multiple time intervals (\sim 15 per cent of time-steps) where the slope reaches and surpasses the SD18 and H18 values.

The Sun is located behind the ascending node of the warp (Chen et al. 2019), which could have an impact on the L_z versus v_z relation. In order to explore how the Sun's location relative to the LONs affects the measured slope, we measure the slope and its evolution

in an 'anti' SN (anti-SN) sample. The sample is located behind the descending node of the warp, i.e. $\phi_w = 162.5^{\circ}$ (blue solid line in Fig. 16). We observe that the slope at the anti-SN location oscillates about $a \sim -0.5 \times 10^3 \, \mathrm{kpc^{-1}}$. More than half of the slope values are now negative and the SD18 and H18 values are reached (or exceeded) in only a third of the time as the SN sample (≤ 6 per cent of timesteps). However, when considering the negative of the slope in SD18 and H18 (orange dotted line), the anti-SN sample reaches that value at the same rate as the SN sample reaches the real value.

We conclude that the bending waves produced by misaligned gas accretion along the warp in the simulation are able to produce similar trends as found by SD18 and H18 in the MW. The large positive values of the slope found by SD18 and H18 are not unusual given the Sun's position relative to the LONs of the warp.

4.5 Propagation of the bending waves

In Sections 4.2 and 4.4, we established the presence of bending waves, their pattern speeds throughout the disc, and their consequences on vertical kinematics in a simulated SN. We now explore the time evolution of $\langle z \rangle$ distribution of stars in cylindrical sectors. We use sectoral bins that are non-overlapping with $\Delta\phi_w=12^\circ$ in each ring. This analysis is a counterpart of the frequency analysis but in real space, which aids in understanding the observational consequences of the waves found in Section 4.2.

4.5.1 Warped simulation

For the warped simulation, the left column of Fig. 17 shows the evolution of $\langle z \rangle$ in 1 kpc-wide rings from 5.5 to 10.5 kpc (rows), starting at t=10 Gyr with time-steps $\delta t=10$ Myr. The horizontal green line shows the location of the SN in the MW (Chen et al. 2019). The diagonal black lines are the most prominent frequencies of the bending waves taken from Figs 8 (bottom right) and 9 (right) for this time interval. The values of the frequencies are indicated in the legend at the top of Fig. 17.

The distributions of $\langle z \rangle$ at any time are dominated by an m=1 angular dependence; i.e. at each annulus and time interval, $\langle z \rangle$ has a single peak (red) and trough (blue). Over time, the bend propagates in a retrograde direction, i.e. in the direction of decreasing ϕ_w . The pattern speed of the retrograde bending wave (solid, black line), identified in Fig. 9, matches the slope of the m=1 signal in the $\langle z \rangle$ distribution at all radii. This coincidence of slopes is in agreement with Fig. 8, which shows that the $\Omega_{\rm p} \approx -13\,{\rm km\,s^{-1}\,kpc^{-1}}$ bending wave is spread across those radii.

Superposed on the overall m=1 bending wave, we can also see individual bending wave packets (which we loosely refer to as 'ripples' to distinguish their particular behaviour) that propagate to increasing ϕ_w , i.e. in the direction of rotation. These ripples are probably the result of constructive interference between the more prominent retrograde m=1 bending waves and the less powerful prograde m=1 and 2 bending waves. In Fig. 8, we identify the prominent prograde m=1 ($\Omega_p\approx 43\,\mathrm{km\,s^{-1}\,kpc^{-1}}$) and m=2 ($\Omega_p\approx 15\,\mathrm{km\,s^{-1}\,kpc^{-1}}$) bending wave pattern speeds and overlay them on top of the $\langle z \rangle$ maps at each radius. The prograde pattern speeds appear to match the slopes of the ripples at each radial interval. Figs 8 and 9 demonstrate that there are more frequencies present in the warped

 $^{^{1}}$ We remind the reader of the equivalence of the angles 360° and 0° , i.e. that the top end of each panel wraps back to the bottom.

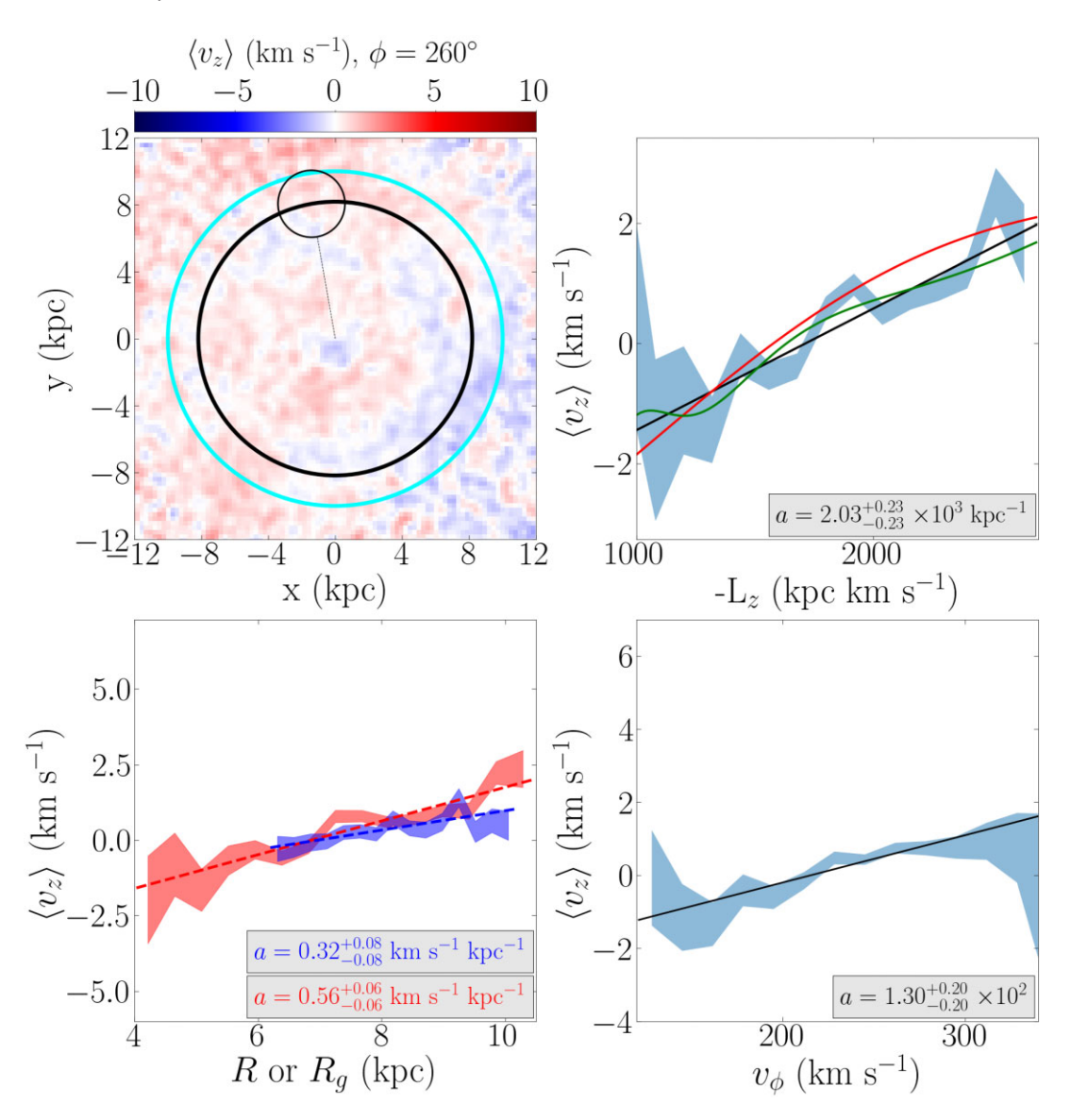


Figure 14. Similar to Fig. 12 but for the unwarped model at 11.8 Gyr. Top left: Distribution of $\langle v_z \rangle$ of the stellar disc. The small black circle indicates a region of radius 2 kpc to simulate an SN (azimuth indicated above the colour bar). The solid black and cyan lines represent the solar annulus, R = 8.18 and 10 kpc, respectively. A Gaussian filter has been applied to the colour distribution with a standard deviation set to $\sigma = 1$ pixel $= 260 \times 260$ pc. Top right: Binned distribution of $\langle v_z \rangle$ as a function of the angular momentum, L_z , in the SN sample of the unwarped model. The shaded region shows the standard deviation of $\langle v_z \rangle$ in each bin. There are three model fits present: linear (black line), sinusoidal (red line), and wrapping (green line). Bottom left: Binned distributions of $\langle v_z \rangle$ as functions of radii, R (blue lines), and guiding radii, R_g (red lines), in the same SN sample. Each distribution has a fitted linear model (dashed lines). Bottom right: Binned distribution of $\langle v_z \rangle$ as a function of $v_z \rangle$ in the same SN sample. The distribution has a fitted linear model (black line). The slopes of the fitted linear models are shown in the bottom right corners of the respective panels.

simulation that could contribute to the constructive interference, but due to their smaller power, we do not include them in the $\langle z \rangle$ maps.

4.5.2 Unwarped simulation

We perform the same analysis on the unwarped model in Fig. 17 (right) with an identical set-up of cylindrical bins and time interval. The diagonal black lines are the most prominent frequencies of the m=1 and 2 bending waves taken from Figs 6 (bottom right) and 7 (right) for the 10-12 Gyr time interval. The values of the frequencies are indicated in the legend at the top of Fig. 17.

The distributions of $\langle z \rangle$ for the unwarped simulation show no dominant signal but a superposition of multiplicities with ampli-

tudes that are weaker by a factor of 5 than those in the warped model (note the different colour scale). The most recognizable signals are a prograde m=2 (t=10.5 Gyr), a retrograde m=1 (11.0 Gyr $\leq t/$ Gyr ≤ 11.5 Gyr), and an m=0 (t=10.25 Gyr) signal. From Figs 6 and 7, we determine the pattern speeds of the most prominent bending waves and overlay them on top of the $\langle z \rangle$ distribution. The bending waves with the most power are the retrograde m=1 (solid) and prograde m=2 (dotted) with $\Omega_p \approx -13$ and $12 \, \mathrm{km \, s^{-1} \, kpc^{-1}}$, respectively. These bending waves seemingly match the slopes of the m=1 and 2 signals in the $\langle z \rangle$ distribution at all radii, e.g. at t=11.0 and 10.2 Gyr, respectively. We observe additional bending waves in Figs 6 and 7 that have less power, e.g. the prograde m=1 wave with $\Omega_p \approx 24 \, \mathrm{km \, s^{-1} \, kpc^{-1}}$.

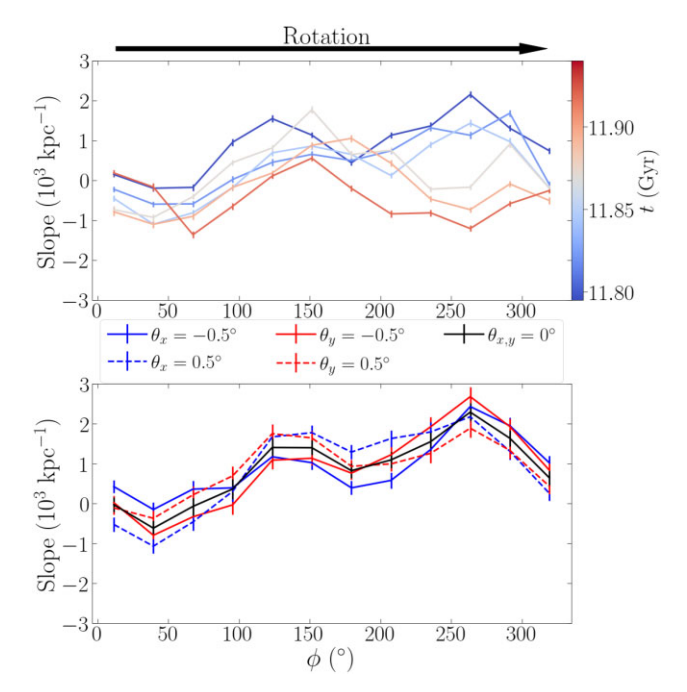


Figure 15. Slope of the $\langle v_z \rangle - L_z$ relation with azimuth for SN samples in the unwarped model. Top panel: 5 times separated by 20 Myr (colours). Bottom panel: slope variation, for the unwarped model at 11.8 Gyr, when the largest slope is observed, with different artificial tilts about the *x*-axis (red lines), about the *y*-axis (blue lines), and without any artificial tilt (black line). Note that the range of the *y*-axis for both panels is almost a third of that in Fig. 13. This demonstrates that if the mid-plane were defined inaccurately, the resulting small tilts would not produce the large slopes measured in the MW or in the warped model.

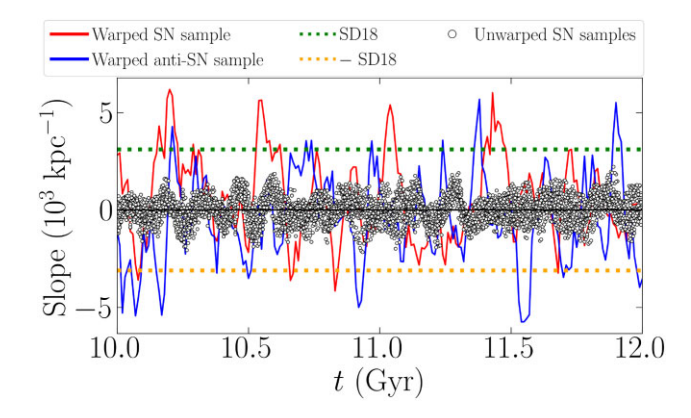


Figure 16. Evolution of the slope of the $\langle v_z \rangle - L_z$ relation for all SN samples in the unwarped model (open circles) and SN samples in the warped model at $\phi_w = -17.5^\circ$ (red) and $\phi_w = 162.5^\circ$ (blue). The samples are spheres centred on $R = 8.18\,\mathrm{kpc}$ and with $r = 2\,\mathrm{kpc}$. The green dotted line shows the SN slope value (SD18), while the orange dotted line is the negative of that value. In the unwarped model, the mean and overall slope values do not generally exceed $2\times10^3\,\mathrm{kpc}^{-1}$ in the span of $2\,\mathrm{Gyr}$ and at any SN sample. In the warped model, the slope regularly matches, or exceeds, the MW value.

When overlaying this pattern speed on top of the $\langle z \rangle$ distribution, we observe some coincidences with the slopes of ripples. We again speculate that the visible signals in the $\langle z \rangle$ distribution are caused by constructive interference.

4.5.3 Bending waves in the SN

After uncovering the complex bending signatures of the warped model in Fig. 17, we test whether the peaks of the bending waves correlate with large slope values examined in Section 4.4. Higher positive slope values are likely to manifest when a $\langle v_z \rangle$ peak (red) of a bending wave is passing through the SN. In Fig. 18, we use the same sectoral bins implemented in Fig. 17 to measure the evolution of $\langle z \rangle$ (top) and the slope of the $L_z - \langle v_z \rangle$ relation (bottom) in each azimuthal bin at $7.18 \le R/\text{kpc} \le 9.18$ (solar annulus). We indicate the SN and anti-SN samples with a shaded grey line centred on $\phi_w = -17.5^\circ$ and 162.5° (Chen et al. 2019), respectively, with an azimuthal range of $\delta \phi_w = 25^\circ$. At each time interval, we fit equation (18) to the $L_z - \langle v_z \rangle$ distribution in each azimuthal bin; when the slope of the fit is greater than the one measured by SD18 and H18, the time interval is indicated with a black vertical line.

The slope in the $L_z - \langle v_z \rangle$ of the SN appears to exceed the SD18 and H18 values when the SN has a peak in $\langle v_z \rangle$. The slope distribution in the bottom panel demonstrates that the peaks correlate with $a \gtrsim 1 \times 10^3 \, \mathrm{kpc^{-1}}$. No time interval with a trough (blue) in the SN sample has a slope that exceeds the observed value, and they are mostly negative. The anti-SN has fewer positive slopes and more regions with negative slopes that reach $a \lesssim -3.05 \times 10^3 \, \mathrm{kpc^{-1}}$ (vertical magenta lines) with a similar frequency as the SD18 and H18 values are reached in the SN sample. Further analysis of earlier times indicates that this inversion is not present in both SN and anti-SN samples, but rather reaches the SD18 and H18 and their negative values at similar rates. The inversion at $10 \le t/ \, \mathrm{Gyr} \le 12$ is likely the result of gas flux variations between the North (z>0) and South (z<0) sides of the warp and not due to the location of our samples.

The slope evolution demonstrates that regions of $a \gtrsim 3.05 \times 10^3 \, \mathrm{kpc^{-1}}$ and $a \lesssim -3.05 \times 10^3 \, \mathrm{kpc^{-1}}$ propagate through the entire solar annulus in a retrograde fashion, mirroring the dominant m=1 signal found in Fig. 17. Additionally, the ripples in the $\langle z \rangle$ (Fig. 17) and $\langle v_z \rangle$ distributions (that we interpret as the result of constructive interference) are also present in the slope evolution. The results of this analysis can be interpreted as a direct link between the high slope values observed in SD18 and H18 and the bending waves manifesting from the warp's perturbation.

4.6 The effect of stellar ages

The dispersion relation of equation (16) applies to WKB waves in kinematically cold discs, i.e. in the absence of in-plane velocity dispersion. In real discs, scattering at inner and outer Lindblad resonances and with giant molecular clouds increases the orbital eccentricity of stars, making populations kinematically hotter over time (see e.g. Sellwood 2014, for a review). Toomre (1966) derived the dispersion relation of small-amplitude bending waves $h(x, t) = He^{i(kx - \omega t)}$ propagating in an infinite, thin slab of stars

$$\omega^2 = 2\pi G \Sigma(R)|k| - \sigma_r^2 k^2, \tag{21}$$

where σ_x is the in-plane velocity dispersion in the x-direction and Σ is the vertically integrated surface density of the slab. Similar to equation (16), the term $2\pi G\Sigma(R)|k|$ represents the gravitational restoring force brought on by the bend, while $\sigma_x^2 k^2$ is a destabilizing inertial term. This dispersion relation demonstrates that disturbances with shorter wavelengths (large k) are unstable as they outweigh the restoring force, which translates to an exponential growth of the h(x, t) distortion.

The assumption of an infinite, thin slab of stars cannot be applied to real galaxies, but it provides a useful estimate of how the propagation

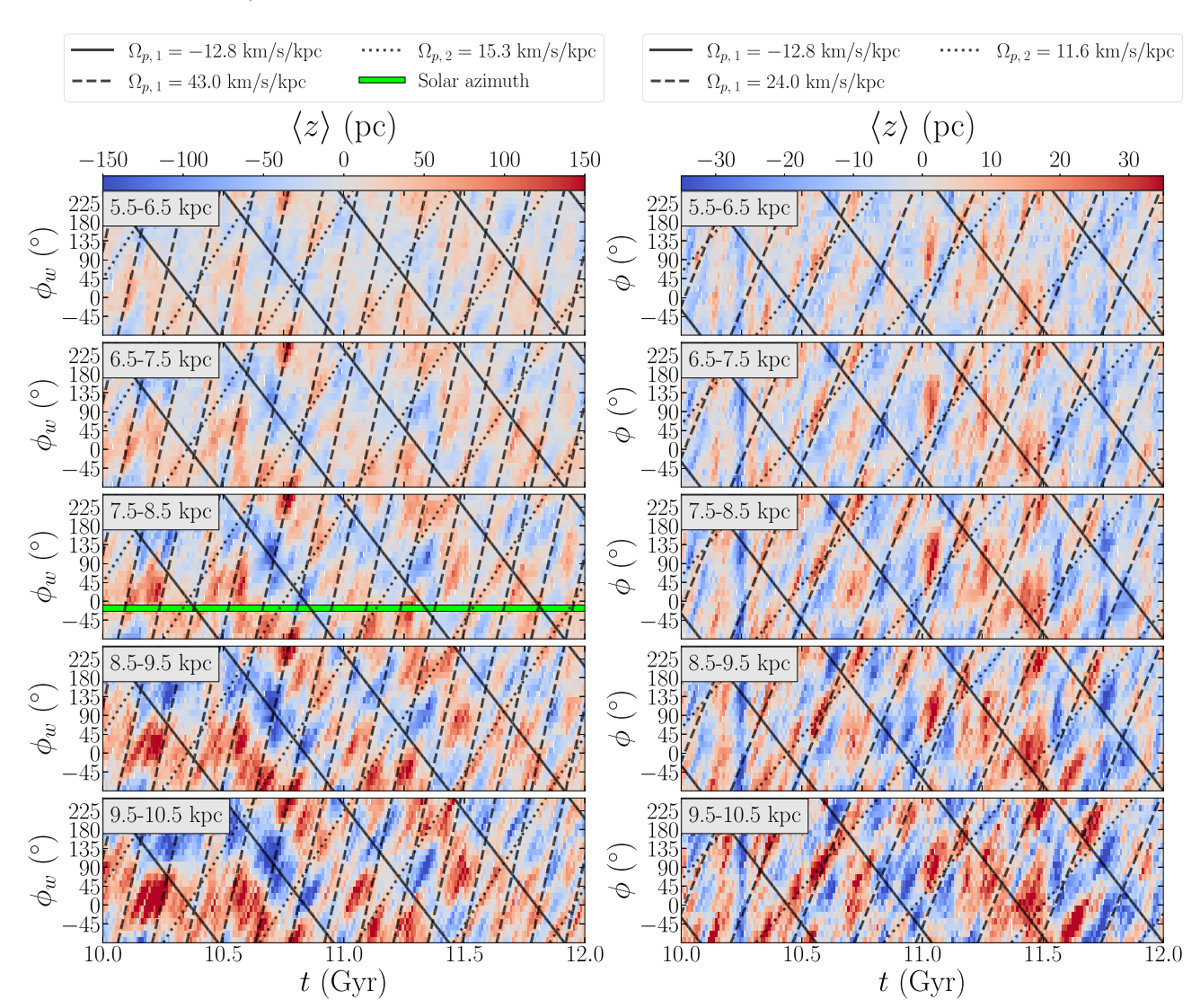


Figure 17. Evolution of the stellar mean height above the mid-plane, $\langle z \rangle$, in the warped (left) and unwarped (right) simulations. The horizontal solid green line represents the solar azimuth relative to the ascending node of the warp's LON (Chen et al. 2019). The diagonal black lines correspond to the most prominent retrograde m = 1 (solid) and prograde m = 1 (dashed) and m = 2 (dotted) bending pattern speeds present in the 10–12 Gyr interval (see Figs 7 and 9).

of bending waves is affected by the in-plane velocity dispersion. For the purpose of this analysis, we substitute σ_x in equation (21) with the in-plane radial velocity dispersion, σ_R . For a disc with a given σ_R , bending waves are able to propagate provided k is smaller than the cut-off value, which ensures that the right-hand side of equation (21) remains positive. As σ_R rises, this critical k needs to decrease. While this holds for discs with different σ_R , we might suspect that, within a given disc, kinematically hotter populations will not be able to support short-wavelength bending waves. For any wave packet, which is constructed by the superposition of sinusoidal waves of varying wavelengths, the shorter wavelengths may only be supported by the kinematically coolest populations. As such, the wave packet might be expected to be sharper in cooler populations, and more gently varying in the hotter populations. As σ_R rises with stellar age in a stellar disc, we test whether the bending waves are sharper in younger populations.

The top row of Fig. 19 presents the distributions of $\langle z \rangle$ at t=10.8 Gyr for populations separated by stellar age, in four equally populated bins. The distributions are presented for stars formed in the main disc only, in order to avoid warp stars that can take up to \sim 6 Gyr

to fully settle and phase mix into the disc (Khachaturyants et al. 2021). Besides the overall m=1 bend, we observe strong bending waves, in the $\langle z \rangle$ distributions (coherent red and blue structures). These bending waves reach as far inside the disc as R=4 kpc in the youngest population, with amplitudes of ~ 100 pc. More importantly, the bending waves, while strongest in the young populations, can be recognized in all populations. The bending waves in the youngest population are also the sharpest ones, whereas the waves in the older populations become less sharp at short wavelengths. Thus, in the old populations, Fig. 19 reveals a coherent large-scale signal but not so much the small-scale patterns present in the young populations.

In order to aid in comparing with observational data, for which stellar ages have high uncertainties (Sanders & Das 2018), we split the stars formed in the main disc by their radial actions, J_R . The radial action of a star characterizes the extent of radial oscillations of a star's orbit and is thus a proxy for the in-plane velocity dispersion. The bottom row of Fig. 19 presents the distributions of $\langle z \rangle$ separated by J_R in bins containing an equal number of stars. Bending waves become less sharp with increasing values of J_R , similar to the age cuts in Fig. 19.

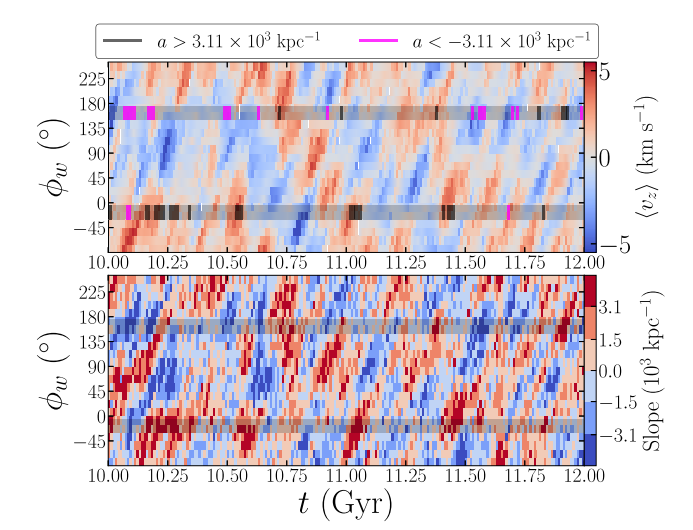


Figure 18. Evolution of the mean vertical velocity, $\langle v_z \rangle$ (top), and the slope of the $L_z - \langle v_z \rangle$ relation (bottom) in the radial interval $7.18 \le R/\ker \le 9.18$ of the warped simulation. The horizontal shaded lines indicate a simulated SN ($\phi_w = -17.5^\circ$) and anti-SN ($\phi_w = 162.5^\circ$) samples in which the slope of the $L_z - \langle v_z \rangle$ is measured at each time interval. The vertical black lines indicate where the slope of the $L_z - \langle v_z \rangle$ relation is equal or exceeds the slope as measured by SD18 and H18. In the top panel, the vertical magenta lines indicate where the slope of the $L_z - \langle v_z \rangle$ relation is equal or less than the negative of this observed value. We observe that large positive and negative slopes are correlated with the peaks and troughs of bending waves, respectively.

As the age and $J_{\rm R}$ bins are equally populated, we expect similar levels of Poisson noise and therefore equally sharp bending waves if their sharpness was only noise limited; however, there is a clear difference between these populations. This implies that the kinematically hottest populations are unable to support the shortest wavelengths.

For a quantitative demonstration that bending waves are sharper in kinematically cooler populations, we note that short wavelengths correspond to larger Fourier m terms compared to long wavelengths. Thus, bending wave power should be concentrated in lower Fourier m components in hot populations compared with cool ones. We analyse the Fourier amplitudes of the vertical displacement for the shaded populations in Fig. 19. We calculate the amplitudes using equation (9) for $m \in [1, 7]$ in 50 sequential snapshots, which corresponds to the time interval 10.5 Gyr $\leq t/$ Gyr ≤ 11.0 . The centre-left panel of Fig. 17 shows that a clear m = 1 bending wave is present in this region at this time. We avoid larger m values since these mostly capture noise in the vertical distribution. In order to intercompare the different populations, the amplitudes are averaged over the 500 Myr time interval and then normalized by their m = 1 amplitudes. In this way, the difference in the overall bending wave strength in the different populations is factored out. The variation of the normalized vertical displacement amplitudes, A_z , with multiplicity is presented in Fig. 20, with the shaded regions representing the standard deviation of A_z . The amplitude of the vertical displacement decreases more rapidly with m for increasing age and J_R populations, indicating that the bending wave power is restricted to large wavelengths in the kinematically hot populations and confirming that the bending waves are sharper in the cool, young populations and smoother in the hotter, old ones. This agrees with the visual impression of the waves given by Fig. 19. We have repeated this analysis at a wide range of radii and times and have confirmed that in the vast majority of cases the power is restricted to smaller m in hot populations compared with cooler ones.

5 SUMMARY

In this paper, we have analysed the bending waves that appear in simulations with no recent interactions. One of these simulations develops a warp via continuous misaligned gas accretion. We demonstrated that both simulations exhibit bending waves. However, the presence of the warp produced significantly stronger bending waves, as well as more substantial power in prograde bending waves.

- (i) The warped model produces both retrograde and prograde bending waves; the latter would normally decay rapidly, but are continuously re-excited throughout the model's evolution. Bending waves in the unwarped model are significantly weaker in amplitude when compared to the warped model. The prograde waves are damped with time, while the retrograde waves are long-lived. The pattern speeds of the bending waves in both simulations are consistent with theoretically expected 'forbidden regions' for bending waves.
- (ii) The irregular gas inflow in the warped simulation is the source of the perturbations exciting the stronger bending waves, with the flux of cold gas correlated to the strength of the bending waves of the disc. The flux varies substantially over time and on a wide range of frequencies. Cross-correlation analysis between the flux and vertical power at two annuli revealed a lag indicative of an inward-propagating bending wave. The group velocity estimated from the time lag is very similar to the radial group velocity obtained from the WKB approximation.
- (iii) In the simulated SN sample of the warped model, the slope of the $L_z \langle v_z \rangle$ relation reaches and exceeds the values observed in the SN (SD18). The slope shows a wave-like dependence on azimuth with the wave propagating in a prograde direction. Since the warp is fixed in our analysis, this indicates that the slope is a result of propagating bending waves and not a direct imprint of the warp. In the unwarped simulation, the smaller bending wave amplitudes result in weaker slopes of the $L_z \langle v_z \rangle$ relation; however, the slopes still reach ~ 60 per cent of the SD18 values.
- (iv) In the warped simulation, bending waves are present in stellar populations of all ages. The strongest and sharpest waves in $\langle z \rangle$ are in the youngest populations, while older ones are less sharp. The same trends are observed when splitting populations by the radial action.
- (v) The azimuthal $\langle z \rangle$ distribution in the warped model exhibits a strong, retrograde, m=1 bend, extending inwards to at least R=5 kpc. We also find localized prograde bending waves, which we term ripples. The overlaid frequencies from the spectral analysis match the slopes of m=2 and 1 prograde ripples, suggesting that they are the result of constructive interference between the prograde waves and the long-lived retrograde m=1 bending wave.

In conclusion, our results demonstrate the role of misaligned gas accretion as a continuous source of vertical perturbations and the excitation of bending waves in galactic discs. This process may also contribute to the vertical perturbations and out-of-equilibrium features observed in the SN.

ACKNOWLEDGEMENTS

VPD, LBS, and TK are supported by STFC consolidated grant #ST/R000786/1. We thank the referee of this paper, James Binney, for comments that helped improve the paper. The simulations in this paper were run at the DiRAC Shared Memory Processing System at the University of Cambridge, operated by the COSMOS Project at

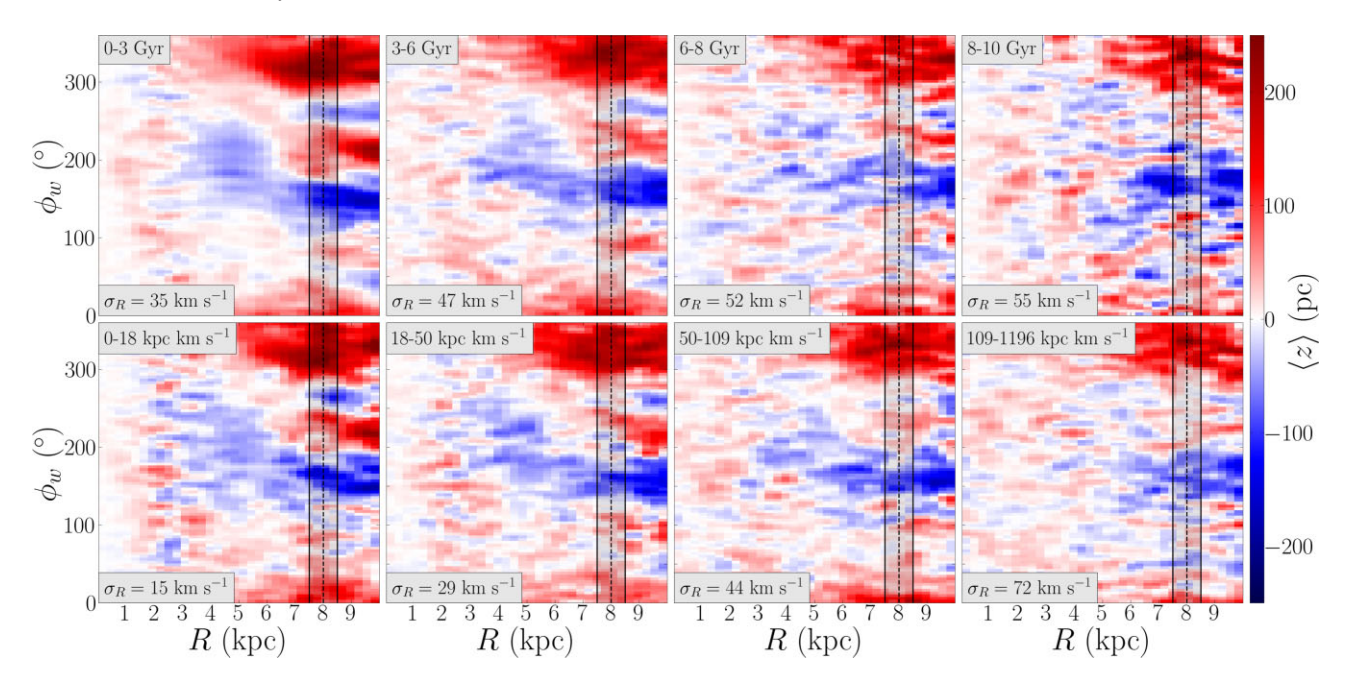


Figure 19. Cylindrical distributions of $\langle z \rangle$ for populations in different age (top) and radial action, J_R (bottom), ranges in the warped model at 10.8 Gyr (age and J_R ranges annotated in the top left of each panel). The bottom left of each panel shows the radial velocity dispersion, σ_R , in the solar annulus sample of each age and J_R cuts (shaded region). The sense of rotation is towards increasing ϕ_w , where $\phi_w = 0^\circ$ represents the ascending node of the warp's LON. A bending wave is visible in all populations but is strongest, and most clearly defined, in the youngest and low- J_R populations. A Gaussian filter has been applied to the colour distribution in each panel with a standard deviation of the Gaussian kernel set to $\sigma = 1$ pixel = 570 pc × 570 pc.

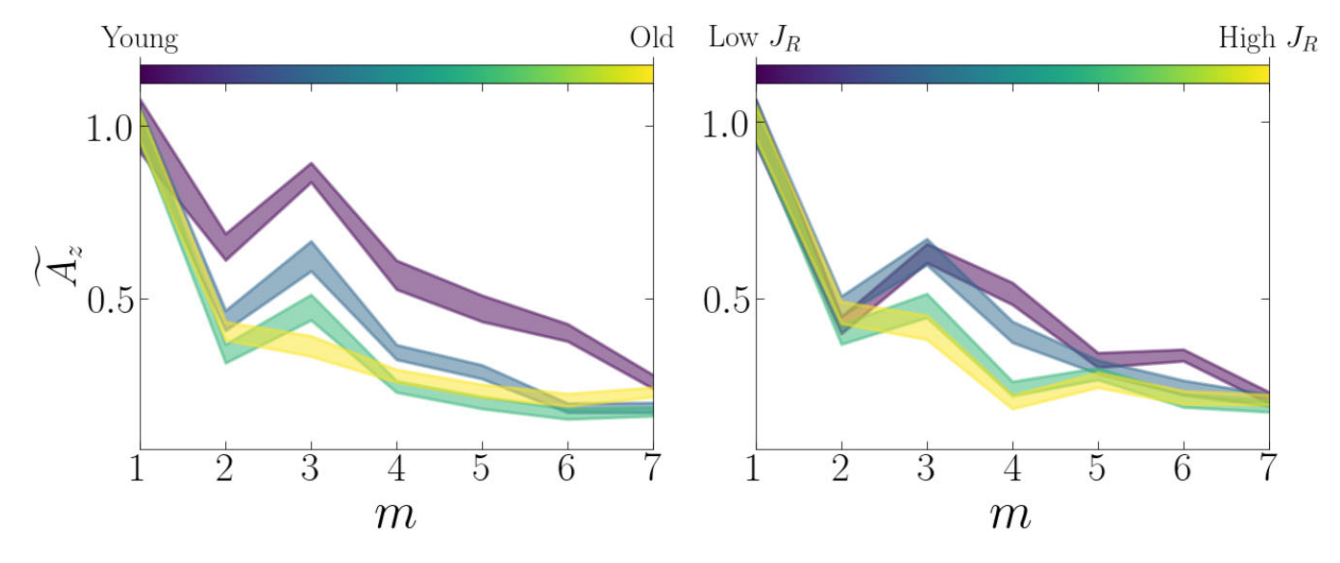


Figure 20. Relationship between normalized vertical displacement amplitudes, $\widetilde{A_z}$ (see equation 9), and their respective Fourier multiplicities, m. The Fourier amplitudes are calculated for the different stellar populations presented in the shaded region of Fig. 19. In order to reduce the effect of noise, the amplitudes are calculated for 50 sequential snapshots ($\Delta t = 500 \,\mathrm{Myr}$), averaged over the entire time interval, and finally normalized by $\widetilde{A_z}(m=1)$. The shaded region shows the standard deviation of $\widetilde{A_z}$.

the Department of Applied Mathematics and Theoretical Physics on behalf of the STFC DiRAC HPC Facility (www.dirac.ac.uk). This equipment was funded by BIS National E-infrastructure capital grant ST/J005673/1, STFC capital grant ST/H008586/1, and STFC DiRAC Operations grant ST/K00333X/1. DiRAC is part of the National E-Infrastructure. Analysis was carried out on Stardynamics, a 64-core machine that was funded from Newton Advanced Fellowship NA150272 awarded by the Royal Society and the Newton Fund. All of the simulation processing was performed with the PYTHON

library PYNBODY (Pontzen et al. 2013). The authors thank Rok Roškar for providing us with his code for producing spectrograms and Sarah Loebman for suggesting using this code for the bending wave spectrum.

DATA AVAILABILITY

The simulation data set used here can be shared for limited use on request to VPD (vpdebattista@gmail.com).

REFERENCES

Agertz O., Teyssier R., Moore B., 2009, MNRAS, 397, L64

Antoja T. et al., 2018, Nature, 561, 360

Aumer M., White S. D. M., 2013, MNRAS, 428, 1055

Aumer M., White S. D. M., Naab T., Scannapieco C., 2013, MNRAS, 434, 3142

Bennett M., Bovy J., 2021, MNRAS, 503, 376

Binney J., May A., 1986, MNRAS, 218, 743

Binney J., Schönrich R., 2018, MNRAS, 481, 1501

Binney J., Tremaine S., 2008, Galactic Dynamics, 2nd edn. Princeton Univ. Press, Princeton, NJ

Binney J., Jiang I.-G., Dutta S., 1998, MNRAS, 297, 1237

Bland-Hawthorn J., Tepper-García T., 2021, MNRAS, 504, 3168

Bland-Hawthorn J. et al., 2019, MNRAS, 486, 1167

Briggs F. H., 1990, ApJ, 352, 15

Bullock J. S., Dekel A., Kolatt T. S., Kravtsov A. V., Klypin A. A., Porciani C., Primack J. R., 2001, ApJ, 555, 240

Carlin J. L. et al., 2013, ApJ, 777, L5

Chen X., Wang S., Deng L., de Grijs R., Yang M., 2018, ApJS, 237, 28

Chen X., Wang S., Deng L., de Grijs R., Liu C., Tian H., 2019, Nat. Astron., 3, 320

Chequers M. H., Widrow L. M., 2017, MNRAS, 472, 2751

Chequers M. H., Widrow L. M., Darling K., 2018, MNRAS, 480, 4244

Darling K., Widrow L. M., 2019, MNRAS, 484, 1050

Debattista V. P., van den Bosch F. C., Roškar R., Quinn T., Moore B., Cole D. R., 2015, MNRAS, 452, 4094

Debattista V. P., Gonzalez O. A., Sand erson R. E., El-Badry K., Garrison-Kimmel S., Wetzel A., Faucher-Giguère C.-A., Hopkins P. F., 2019, MNRAS, 485, 5073

Dehnen W., 1998, AJ, 115, 2384

Dekel A., Shlosman I., 1983, in Athanassoula E., ed., Proc. IAU Symp. 100, Internal Kinematics and Dynamics of Galaxies. D. Reidel Publishing Co., Dordrecht, p. 187

Earp S. W. F., Debattista V. P., Macciò A. V., Cole D. R., 2017, MNRAS, 469, 4095

Earp S. W. F., Debattista V. P., Macciò A. V., Wang L., Buck T., Khachaturyants T., 2019, MNRAS, 488, 5728

Efremov Y. N., Ivanov G. R., Nikolov N. S., 1981, Ap&SS, 75, 407

Faure C., Siebert A., Famaey B., 2014, MNRAS, 440, 2564

Feldmann R., Spolyar D., 2014, MNRAS, 446, 1000

Fiteni K., Caruana J., Amarante J. A. S., Debattista V. P., Beraldo e Silva L., 2021, MNRAS, 503, 1418

Foreman-Mackey D., Hogg D. W., Lang D., Goodman J., 2013, PASP, 125, 306

Fox A. J., Richter P., Ashley T., Heckman T. M., Lehner N., Werk J. K., Bordoloi R., Peeples M. S., 2019, ApJ, 884, 53

Friske J. K. S., Schönrich R., 2019, MNRAS, 490, 5414

Gaia Collaboration, 2016a, A&A, 595, A1

Gaia Collaboration, 2016b, A&A, 595, A2

Gaia Collaboration, 2018, A&A, 616, A11

Gómez F. A. et al., 2012, MNRAS, 423, 3727

Gómez F. A., White S. D. M., Grand R. J. J., Marinacci F., Springel V., Pakmor R., 2017, MNRAS, 465, 3446

Huang Y. et al., 2018, ApJ, 864, 129

Hunter C., Toomre A., 1969, ApJ, 155, 747

Ibata R. A., Razoumov A. O., 1998, A&A, 336, 130

Jiang I.-G., Binney J., 1999, MNRAS, 303, L7

Kazantzidis S., Zentner A. R., Kravtsov A. V., Bullock J. S., Debattista V. P., 2009, ApJ, 700, 1896

Kerr F. J., 1957, AJ, 62, 93

Khachaturyants T., Beraldo e Silva L., Debattista V. P., 2021, MNRAS, 508, 2350

Khoperskov S., Di Matteo P., Gerhard O., Katz D., Haywood M., Combes F., Berczik P., Gomez A., 2019, A&A, 622, L6

Laporte C. F. P., Minchev I., Johnston K. V., Gómez F. A., 2019, MNRAS, 485, 3134

Levine E. S., Blitz L., Heiles C., 2006, ApJ, 643, 881

Li Z.-Y., Shen J., 2020, ApJ, 890, 85

López-Corredoira M., Abedi H., Garzón F., Figueras F., 2014, A&A, 572, A101

Merritt D., Sellwood J. A., 1994, ApJ, 425, 551

Miller G. E., Scalo J. M., 1979, ApJS, 41, 513

Navarro J. F., Frenk C. S., White S. D. M., 1996, ApJ, 462, 563

Nelson R. W., Tremaine S., 1995, MNRAS, 275, 897

Ostriker E. C., Binney J. J., 1989, MNRAS, 237, 785

Pontzen A., Roškar R., Stinson G. S., Woods R., Reed D. M., Coles J., Quinn T. R., 2013, Astrophysics Source Code Library, record ascl:1305.002

Raha N., Sellwood J. A., James R. A., Kahn F. D., 1991, Nature, 352, 411

Reed B. C., 1996, AJ, 111, 804

Roškar R., Debattista V. P., Brooks A. M., Quinn T. R., Brook C. B., Governato F., Dalcanton J. J., Wadsley J., 2010, MNRAS, 408, 783

Roškar R., Debattista V. P., Quinn T. R., Wadsley J., 2012, MNRAS, 426, 2089

Sanders J. L., Das P., 2018, MNRAS, 481, 4093

Schönrich R., Dehnen W., 2018, MNRAS, 478, 3809

Sellwood J. A., 1996, ApJ, 473, 733

Sellwood J. A., 2014, Rev. Mod. Phys., 86, 1

Sellwood J. A., Athanassoula E., 1986, MNRAS, 221, 195

Sellwood J. A., Merritt D., 1994, Bull. Am. Astron. Soc., 26, 916

Sellwood J. A., Nelson R. W., Tremaine S., 1998, ApJ, 506, 590

Shen S., Wadsley J., Stinson G., 2010, MNRAS, 407, 1581

Springel V., 2010, ARA&A, 48, 391

Stevens A. R. H., Lagos C. d. P., Contreras S., Croton D. J., Padilla N. D., Schaller M., Schaye J., Theuns T., 2017, MNRAS, 467, 2066

Stinson G., Seth A., Katz N., Wadsley J., Governato F., Quinn T., 2006, MNRAS, 373, 1074

Toomre A., 1966, Notes on the 1966 Summer Study Program in Geophysical Fluid Dynamics at the Woods Hole Oceanographic Institution. Woods Hole Oceanographic Institution, Falmouth, MA

Toomre A., 1983, in Athanassoula E., ed., Proc. IAU Symp. 100, Internal Kinematics and Dynamics of Galaxies. D. Reidel Publishing Co., Dordrecht, p. 177

van den Bosch F. C., Abel T., Croft R. A. C., Hernquist L., White S. D. M., 2002, ApJ, 576, 21

Vasiliev E., 2019, MNRAS, 482, 1525

Velliscig M. et al., 2015, MNRAS, 453, 721

Wadsley J. W., Stadel J., Quinn T., 2004, New Astron., 9, 137

Weaver H., Williams D. R. W., 1974, A&AS, 17, 251

Werk J. K. et al., 2019, ApJ, 887, 89

Widrow L. M., Gardner S., Yanny B., Dodelson S., Chen H.-Y., 2012, ApJ, 750, L41

Williams M. E. K. et al., 2013, MNRAS, 436, 101

Yanny B., Gardner S., 2013, ApJ, 777, 91

This paper has been typeset from a TEX/LATEX file prepared by the author.